

6-30-2016

Platinum Decoupling from PGE in Peridotitic Sulfides from the St. Elena Ophiolite in Costa Rica

Jessica A. Holm
University of South Carolina

Follow this and additional works at: <https://scholarcommons.sc.edu/etd>



Part of the [Geology Commons](#)

Recommended Citation

Holm, J. A.(2016). *Platinum Decoupling from PGE in Peridotitic Sulfides from the St. Elena Ophiolite in Costa Rica*. (Master's thesis). Retrieved from <https://scholarcommons.sc.edu/etd/3524>

This Open Access Thesis is brought to you by Scholar Commons. It has been accepted for inclusion in Theses and Dissertations by an authorized administrator of Scholar Commons. For more information, please contact digres@mailbox.sc.edu.

Platinum decoupling from PGE in peridotitic sulfides from the St. Elena ophiolite in
Costa Rica

by

Jessica A. Holm

Bachelor of Science
University of South Carolina, 2014

Submitted in Partial Fulfillment of the Requirements

For the Degree of Master of Science in

Geological Sciences

College of Arts and Sciences

University of South Carolina

2016

Accepted by:

Michael Bizimis, Director of Thesis

Gene Yogodzinski, Reader

Esther Schwarzenbach, Reader

Lacy Ford, Senior Vice Provost and Dean of Graduate Studies

© Copyright by Jessica A. Holm, 2016
All Rights Reserved.

Acknowledgements

I would like to thank my advisor, Michael “Tightpants” Bizimis, for his extreme patience, guidance, and good humor. Thank you to my committee, Esther Schwarzenbach and Gene Yogodzinski, for the advice and probing which they provided and I needed. Thank you to Dionysis Foustoukos for all his help at Carnegie, whether it was SEM work, driving in the DC area, or thermodynamic quandries. Thank you to Carl Frisby, for showing me the ropes in so many ways. Thank you to Dr. Alan Brandon for (1) having my back when I presented this work at AGU and (2) analyzing these samples first on his (at the time) very brand new MS. Thank you also to Esteban Gazel, because the St. Elena ophiolite is his baby and this work could not have been done in the first place without him. A big thank you also goes to my family, especially my mom, as she inspired my love of science.

Abstract

The platinum group elements (Os, Ir, Ru, Rh, Pt, Pd) are important petrogenetic tracers of mantle processes and the Re-Os isotope system an important tool for tracing ancient depletion and refertilization processes in the mantle. A key characteristic of these elements is that they are siderophile and chalcophile, and their abundance in the Earth's mantle is thought to be controlled by sulfides. Existing thermodynamic data suggests that at reducing conditions similar to those found at the early stages of serpentinization, PGE may exist as alloys in the mantle. While numerous studies report on the bulk peridotite PGE and sulfide PGE systematics, the effects of serpentinization on PGE systematics have not yet been investigated. This study presents bulk rock and in situ (LA-ICPMS on sulfides, down to a 10 micron beam size) PGE concentrations on five partially serpentinized peridotites from the St. Elena ophiolite, Costa Rica. The presence of Fe-Ni alloys and native Cu in these peridotites indicate low fO_2 and fS_2 conditions and low water-rock ratios during serpentinization. Low LREE/HREE ratios, low Ti, and low Al contents in these peridotites suggest variable degrees of depletion (3-14%) with little evidence for melt metasomatism in all but one peridotite. Bulk rock $^{187}\text{Os}/^{188}\text{Os}$ range from 0.1233 to 0.126, consistent with an origin from the depleted upper mantle. Sulfides are dominantly pentlandites. PGE-Re concentrations in sulfides are highly variable, ranging from 1 – 100,000 times that of primitive mantle (PM). PM-normalized PGE-Re patterns in the sulfides are dominated by strong Pt depletions relative to Os, Ir, Ru and

Pd. Bulk rock PGE concentrations are roughly similar to PM, and lack the Pt-depletions seen in sulfides. Mass balance reconstructions using in situ sulfide data and bulk rock sulfide S contents reproduce the measured bulk rock Os, Ir, Ru, concentrations within a factor of 3, but highly underestimate that of Pt. This data suggests that while Os, Ir, and Ru are dominantly hosted in analyzed sulfides, Pt is hosted in other phases but has still remained in the rock within the hand specimen scale. Detailed SEM analyses reveal the presence of various micron-sized Cu-Pt-Pd, Pt-Te, and Pt-Te-Au alloys. Laser ablation data revealed transient Pt spikes within sulfides, further confirming the presence of “nugget” phases that are also enclosed in sulfides. These data demonstrate unambiguously that in serpentinized oceanic peridotites, Pt is not controlled by the sulfide mineralogy. The formation of Pt “nuggets” is likely a subsolidus exsolution feature developed during cooling and pentlandite crystallization. Low sulfur and oxygen fugacities may have helped preserve the Pt alloys, and serpentinization fluids possibly redistributed them, but at scales in the order of millimeters. Finally, the relatively low Pb concentrations in the sulfides are inconsistent with the sulfide solution to the Pb paradox.

Table of Contents

Acknowledgements	iii
Abstract	iv
List of Tables	vii
List of Figures	viii
Chapter 1 Introduction	1
Chapter 2 Geological Setting and Sample Description.....	4
Chapter 3 Analytical Methods	6
Chapter 4 Results	15
Chapter 5 Discussion	45
Chapter 6 Conclusions	63
References.....	65

List of Tables

Table 3.1 Operating parameters.....	10
Table 3.2 RSF for analytical sessions.....	11
Table 3.3 Signal constraints.....	13
Table 4.1.1 Bulk rock trace elements.....	22
Table 4.4.1 Sulfide concentrations.....	23
Table 4.4.2 Average PGE sample concentrations.....	29
Table 4.7.1 Measured bulk rock and reconstructed PGE concentrations	30
Table 4.8.1 Os isotopic compositions.....	31

List of Figures

Figure 3.1 Standard RSF	14
Figure 4.1.1 Bulk rock trace elements	32
Figure 4.1.2 Sulfur vs. Titanium.....	33
Figure 4.2.1 Typical ablated sulfides.....	34
Figure 4.2.2 Sulfides with nuggets	35
Figure 4.3.1 Laser vs. microprobe data.....	36
Figure 4.3.2 Sulfide classification diagram	37
Figure 4.4.1 Sulfide PGE concentrations.....	38
Figure 4.4.2 Pd/Os vs. Copper	39
Figure 4.5.1 Laser ablation spectra	40
Figure 4.6.1 Included sulfide PGE concentrations	41
Figure 4.7.1 Bulk rock PGE concentrations	42
Figure 4.8.1 Os isotopes vs. Re/Os.....	43
Figure 4.9.1 Chalcophile element comparisons	44
Figure 5.1.1 Pt enriched sulfide PGE concentrations	57
Figure 5.1.2 Heterogeneous sulfide in SE10-09	58
Figure 5.1.3 Sulfide Pt/Pt* vs. PGE and chalcophile elements	59
Figure 5.2.1 Bulk rock PGE measurements vs. reconstructions.....	60
Figure 5.3.1 Metasomatic sulfides and Ir/Os fractionation diagrams.....	61
Figure 5.3.2 PGE partition coefficients	62

Chapter 1 Introduction

Platinum Group Elements (PGE: Os, Ir, Ru, Rh, Pt, and Pd) partitioned heavily into Earth's metallic core during core formation due to their highly siderophile nature. The relatively high and approximately chondritic abundances of PGE in the mantle have been explained by the Late Veneer hypothesis, where late delivery of chondritic material added PGE to Earth's primitive mantle after core formation (Kimura et al., 1974; O'Neill, 1990). In the silicate mantle, PGE strongly partition into sulfide phases over silicates. In general, Os, Ir, Ru, and Rh behave compatibly during partial melting, concentrating in mantle sulfide, while Pt, Pd, and Re preferentially partition into sulfide melt phases (Bockrath et al., 2004; Delpech et al., 2012, Lorand et al., 2010). Sulfur is an incompatible element during mantle melting as well. Therefore, melting decreases the abundance of sulfides in the residual mantle. Typical residual sulfide PGE-Re patterns after a partial melting event have high concentrations of Os, Ir, Ru, Rh, and low Pt, Pd, and Re concentrations. In turn, sulfides derived from a mantle melt are enriched in Pt, Pd, and Re compared to Os, Ir, Ru, and Rh. Based on this behavior, PGE are effective geochemical tracers of upper mantle processes such as partial melting, melt percolation, and mantle metasomatism (Alard et al., 2000; Luguet et al., 2001; Lorand et al., 2004, 2008, 2010; Delpech et al., 2012).

The presence of discrete PGE alloys in mantle lithologies has been observed in multiple studies (e.g. Garuti and Zaccarini, 1997; Peregoedova et al., 2004; Li and Ripley, 2006; Luguet et al., 2007). For example, Garuti and Zaccarini (1997) found PGE

alloys forming from low temperature desulfurization during serpentinization of base metal sulfides (BMS, Fe-Ni-Cu mantle sulfides) in chromitites, while others attributed the presence of Ir-Pt rich metal alloys to desulfurization of BMS during melting (Peregoedova et al., 2004; Li and Ripley, 2006; Luguet et al., 2007). On the other hand, Lorand et al. (2008) suggested that Pt-Te-Bi-(Pd) alloy phases in peridotites are produced during subsolidus exsolution of Cu-rich sulfide melt differentiates.

Sometimes, mantle sulfides exhibit strong Pt depletions relative to the other PGE (e.g. Alard et al., 2000; Luguet et al., 2008; Lorand et al., 2010, Foustoukos et al., 2015). Lorand et al. (2008) suggested that this is the result of subsolidus exsolution of a Pt-rich phase since Pt, unlike the remainder of PGE, does not fit in the octahedral site of the lower temperature sulfide variety of pentlandite, due to a lower valence state (Luguet et al., 2001; Lorand et al., 2008). Experimental evidence suggests that in sulfur-poor BMS assemblages, Pt systematically forms separate phases during high temperature crystallization (Peregoedova and Ohnenstetter, 2002), in general agreement with the Lorand et al. (2008) arguments. In turn, Foustoukos et al. (2015) showed that under highly reducing conditions where pentlandite and awaruite minerals coexist, Pt is thermodynamically stable in its native metal form rather than as sulfide. This suggests that both subsolidus cooling and redox conditions may control the decoupling of Pt from PGE in mantle sulfide.

Here I present in situ LA-ICPMS PGE and chalcophile data on peridotitic sulfides combined with bulk rock PGE and trace element data from the St. Elena ophiolite. The presence of awaruite (Ni_{2-3}Fe) and native Cu in these samples implies highly reducing conditions. This allows us to test whether there is a link between melting, subsolidus

equilibration and redox conditions imposed by serpentinization, using sulfide and bulk rock PGE systematics. I will show that a negative Pt anomaly is observed in the majority of sulfides from the St Elena ophiolite. However, this negative Pt anomaly is not present in the bulk rocks, which instead have approximately chondritic patterns and no Pt depletion. Mineralogical evidence supports the decoupling of Pt from other PGE into Pt-alloys. Pt anomalies likely formed during subsolidus exsolution and cooling of primary mantle sulfides. Pt-alloys likely remained extant due to the highly reducing conditions recorded in these samples during serpentinization.

Chapter 2 Geological Setting and Sample Description

The St. Elena ophiolite in Costa Rica is a well-preserved section of a melt-focusing zone in the lithospheric mantle which likely formed along a slow/ultra-slow spreading center (Madrigal et al., 2015). Trace element concentrations of diabase dikes suggest a shallow and garnet-free, depleted MORB-like source of the melts, while the lack of specific enrichments in fluid mobile elements like U and the absence of HFSE depletions relative to the REE (e.g. Nb/La) ratios suggests that interaction with a subduction-related component was minimal at best (Madrigal et al., 2015). The analyzed samples are variably serpentinized peridotites (4 lherzolites and 1 harzburgite; Schwarzenbach et al., 2014). Degree of serpentinization ranges between 30-60% (Schwarzenbach et al., 2016). Sulfide sulfur contents for these peridotites ranges from 55-188 ppm (Schwarzenbach et al., 2016). Sulfides in these serpentinized peridotites are predominantly pentlandites, and nearly all of them are held interstitially in a serpentine matrix (Schwarzenbach et al., 2014; and this study). Opaque mineral assemblages include pentlandite $[(\text{Fe},\text{Ni})_9\text{S}_8]$, magnetite (Fe_3O_4), awaruite (Ni_{2-3}Fe), pyrrhotite (FeS), heazlewoodite (Ni_3S_2), chalcopyrite (CuFeS_2), Cu-pentlandite, native Cu, bornite (Cu_5FeS_4), and other Cu-sulfides (Schwarzenbach et al., 2014). The presence of Fe-Ni alloys such as awaruite, native Cu, and sometimes heazlewoodite in these samples indicates reducing conditions with a relatively low sulfur activity (Schwarzenbach et al., 2014; Foustoukos et al., 2015). Native Cu in a Ni-free sulfide paragenesis is stable below $-15 \log f\text{S}_2$ units and $-30 \log f\text{O}_2$ units at 200°C , 50 MPa and below $-10 \log f\text{S}_2$ units and

-19 log f_{O_2} units at 350⁰C, 50 MPa (Schwarzenbach et al., 2014). Oxygen and sulfur fugacity is further constrained by pentlandite-awaruite equilibrium, where at 50 MPa and 300⁰C, the pentlandite - awaruite paragenesis is stable at approximately -16 to -18 log f_{S_2} units, and -35 to -40 log f_{O_2} units (Foustoukos et al., 2015).

Chapter 3 Analytical Methods

A combination of optical microscopy, Field Emission-SEM, and Laser Ablation-ICPMS are used to characterize the sulfide, alloy mineralization, and in situ PGE-Re-Au-Pb concentrations in the peridotites. Pieces of the whole rock are mounted in epoxy rings and are polished with a Buehler Minimet down to 0.3 μm using Al-oxide powders. The samples are examined with a petrographic microscope for general characterization of sulfide petrography. Samples are then analyzed using a Field Emission-SEM at the Carnegie Institute of Washington (JEOL JSM 6500F), or a Tescan Vega3 SEM or Zeiss Ultra Plus Field Emission-SEM at USC's Electron Microscopy Center to qualitatively identify alloys and sulfide compositions. Spatial resolution down to 100 nm can be achieved with the Field Emission instruments.

LA-ICPMS analysis is done using a Photon Machines UV-Eximer 193nm ArF laser coupled to a THERMOFisher ELEMENT2 HR-ICP-MS at the Center for Elemental Mass Spectrometry, U. of South Carolina. The laser features a HELIX 2 sample cell, through which 0.5-0.9 L/min He carrier gas was run. Nitrogen gas (7-10 mL/min) was introduced to the sample gas mixture in order to increase sensitivity as well as reduce oxide formation and elemental fractionation in the mass spectrometer. Sulfides are ablated at a repetition rate of 5 Hz for 13 seconds with an energy fluence of $\sim 11 \text{ J/cm}^2$, at 100% laser energy. Variable beam sizes are used to match sulfide target; minimum beam size used is 10 μm . Additional operating parameters are given in Table 3.1. If a sulfide is large enough to fit 2 beams of $>10\mu\text{m}$, heterogeneity within single sulfides is then able to

be tested. Any signal contribution from the surrounding silicate can be readily corrected by monitoring Mn, as it is lithophile and held in silicates and not the sulfide or metal alloy phases in the rock, so abnormally high Mn counts were used to screen the analyzed sulfides. It was found that the PGE signal during ablation of the silicates was essentially that of the blank carrier gas, consistent with the well-known control of sulfides on the PGE distribution in the mantle. Therefore, any silicate overlap during ablation only diluted the PGE signal. The peaks ^{34}S , ^{55}Mn , ^{57}Fe , ^{59}Co , ^{60}Ni , ^{63}Cu , ^{66}Zn , ^{75}As , ^{99}Ru , ^{101}Ru , ^{103}Rh , ^{105}Pd , ^{106}Pd , ^{107}Ag , ^{111}Cd , ^{120}Sn , ^{125}Te , ^{185}Re , ^{192}Os , ^{193}Ir , ^{195}Pt , ^{197}Au , and ^{208}Pb were acquired in low resolution mode.

Due to the lack of a widely available homogenous PGE-doped sulfide standard, I developed a method for external LA-ICPMS standardization using a combination of the NIST 612, the iron meteorites Hoba and Filomena, sulfide standard MASS-1, USGS basalt glasses, and an in-house pyrite sample (modified after Sen et al., 2010). Concentrations are calculated by normalization to Fe, which is in turn calculated against the standards using Relative Sensitivity Factors (RSF; reported in Table 3.2) and by summation of all signals to 100% (Gaboardi and Humayun, 2009; Frisby et al., 2016):

$$\text{RSF} = \frac{C_i/C_{\text{Fe}}}{I_i/I_{57\text{Fe}}}$$

Where C_i is the concentration of element i in ppm, and I_i is the blank-corrected intensity for the peak used for that element. Element concentrations for ablated sulfides are calculated using blank-corrected signal intensities and RSF, as follows:

$$C_i = \text{RSF}_i \times \frac{I_i}{I_{\text{Fe}}} \times \frac{1,000,000}{C_{\text{Fe}}}$$

Where RSF_i is the RSF of element i and the Fe concentration of a sulfide is calculated as

$$C_{Fe} = \Sigma(RSF_i \times \frac{I_i}{I_{Fe}})$$

The RSF calculated from different standard materials agree well over a large range of Fe concentrations, for a range of heavy and light elements, and over a variation in matrices (Figure 3.1). RSFs were calculated for each analytical session (typically the beginning of the day). RSF for the suite of elements calculated from our standards are shown in Table 3.2 by analytical session, with the chosen RSF from each standard in bold. A particular standard is preferred for an element when the concentration is known well and counts are relatively high, providing a clear signal with which to calibrate the RSF.

Rh, being monoisotopic and having a significant $^{63}\text{Cu}^{40}\text{Ar}$ interference, has the largest uncertainty associated with its measurement. Both ^{105}Pd and ^{106}Pd are measured in order to tease out $^{65}\text{Cu}^{40}\text{Ar}$ and $^{66}\text{Zn}^{40}\text{Ar}$ interferences. $^{66}\text{Zn}^{40}\text{Ar}$ was calculated using the standard MASS-1, using 215,400 ppm of Zn and an absence of Pd, as the sulfide was not spiked with Pd. For samples with large Cu concentrations, ^{106}Pd is used; for samples with large Zn concentrations, ^{105}Pd is more reliable. $^{61}\text{Ni}^{40}\text{Ar}$ interference on ^{101}Ru are found to be insignificant and therefore no correction is made.

Average detection limits were calculated as 3 standard deviations of the blank signal determined before each sulfide. Detection limits for PGE and chalcophile elements are reported in Table 3.3, along with average signal as a function of concentration. The detection limits reported in Table 3.3 were calculated based on a 15 μm beam size.

Detection limits scale inversely to beam size, therefore a larger beam size would result in lower detection limits.

Bulk rock PGE concentrations and Os isotopes were analyzed at the University of Houston under the supervision of Dr. Alan Brandon.

Bulk rock trace elements were determined by dissolution. Approximately 30 mg of rock powder was spiked with a ^{145}Nd enriched spike and dissolved in 3:1 HF:HNO₃ mixture for 3 days. After repeated dry-downs with HNO₃, the solution was diluted to ~ 500 ppm total dissolved solids. The solutions were analyzed on the ELEMENT2 using a cyclonic spray chamber and an all Teflon nebulizer in self-aspiration mode. The $^{145}\text{Nd}/^{146}\text{Nd}$ ratio, which is free of any major interferences, was used to determine the Nd concentration of the sample by the isotope dilution method. The Nd concentration was then used as the internal standard, and the instrument response (equivalent to the RSF factors for the laser ablation method above) was calculated using the USGS standard BHVO-2 and the preferred concentrations reported in the GEOROC database.

Table 3.1 – Operating Parameters

RF Power (W)	1200
Ar nebulizer flow (L/min)	0.6-0.8
Ar auxiliary gas (L/min)	0.7
Ar cooling gas (L/min)	16
He carrier gas (L/min)	0.5-0.9
N gas (mL/min)	7-10
ThO ⁺ /Th ⁺ (%)	<2
Milliseconds per mass	0.005-0.01
Cones	Ni; H & Sampler

Table 3.2 – RSF for analytical sessions

^10/24/2014						
Element	Hoba	Filomena	Steel	Mass	Pyrite	Final RSF
	50 um	50 um	50 um	25 um	25 um	
S34	0.049	0.020	0.029	1.421	2.301	1.730
Mn55			0.014	0.017		0.017
Fe57	1.000	1.000	1.000	1.000	1.000	1.000
Co59	0.030	0.024	0.029	0.021		0.030
Ni60	0.140	0.113	0.132	0.070		0.140
Cu63	-0.029	0.037	0.027	0.037		0.037
Zn66				0.096		0.096
As75	0.136	0.045	0.050	0.046		0.045
Ru99						0.204
Ru101	0.204	0.084				
Rh103	0.056	0.021				0.056
Pd105	0.147	0.072				0.147
Pd106	0.120	0.065		0.000		0.120
Ag107			0.026	0.024		0.024
Cd111				0.186		0.186
Sn120	0.130	-0.025	0.024	0.028		0.028
Tel25			0.237			0.237
Re185	0.078	0.036				0.078
Os192	0.080	0.026		0.001		0.080
Ir193	0.055	0.020		0.018		0.055
Pt195	0.133	0.045		0.052		0.133
Au197	0.032	0.019	0.025	0.017		0.019
Pb208				0.015		0.015

\$11/15/2014					
Element	Hoba	Filomena	Mass	Pyrite	Final RSF
	50 um	50 um	25 um	25 um	
S34	0.016	0.013	1.028	1.285	1.285
Mn55			0.015		0.015
Fe57	1.000	1.000	1.000	1.000	1.000
Co59	0.025	0.026	0.019	0.000	0.025
Ni60	0.112	0.120	0.065	0.000	0.112
Cu63	0.024	0.049	0.039	0.000	0.039
Zn66			0.078		0.078
As75	0.009	0.039	0.038		0.039
Ru99					0.080
Ru101	0.080	0.086			
Rh103	0.023	0.022			0.023
Pd105	0.075	0.079			0.075
Pd106	0.061	0.066			0.061
Ag107			0.021		0.021
Cd111			0.087		0.087
Sn120	0.057	0.075	0.023		0.023
Tel25					0.268
Re185	0.034	0.037			0.034
Os192	0.033	0.025	0.001		0.033
Ir193	0.023	0.021	0.018		0.023
Pt195	0.058	0.048	0.059		0.058
Au197	0.016	0.021	0.017		0.021
Pb208			0.014		0.014

#1/6/2015							
Element	Hoba	Filomena	Steel	Mass	Pyrite	SL-1G	Final RSF
	50 um	50 um	25 um	25 um	25 um	25 um	
S34	0.054	0.017	0.028	1.200	1.062		1.131
Mn55			0.013	0.015			0.015
Fe57	1.000	1.000	1.000	1.000	1.000	1.000	1.000
Co59	0.026	0.028	0.028	0.021	0.000	0.022	0.027
Ni60	0.124	0.143	0.132	0.071	0.000	0.116	0.133
Cu63	-1.104	0.031	0.026	0.036	0.000	0.038	0.036
Zn66				0.079		0.084	0.079
As75	-0.054	0.037	0.032	0.026		0.031	0.026
Ru99							0.112
Ru101	0.096	0.129					
Rh103	0.028	0.036					0.032
Pd105	0.090	0.121				0.080	0.105
Pd106	0.075	0.109				0.052	0.092
Ag107			0.020	0.018		0.021	0.018
Cd111				0.112		0.100	0.112
Sn120	0.139	0.035	0.021	0.018		0.028	0.018
Te125			0.299			0.171	0.299
Re185	0.035	0.040					0.035
Os192	0.038	0.039		0.001			0.038
Ir193	0.027	0.035		0.014			0.027
Pt195	0.072	0.091		0.052			0.072
Au197	0.047	0.025	0.023	0.015			0.025
Pb208				0.010		0.015	0.010

*11/7/2015							
Element	Hoba	Filo	Mass	Steel	Pyrite	BIR	Final RSF
	50 um	50 um	5 um	50 um	15 um	50 um	
	Lines	Lines	Spots	Spots	Spots	Spots	
S34	0.101	0.026	2.061	0.296	5.179		5.179
Mn55			0.015	0.020			0.020
Fe57	1.000	1.000	1.000	1.000	1.000	1.000	1.000
Co59	0.026	0.026	0.017	0.030		0.024	0.026
Ni60	0.100	0.092	-0.015	0.127		0.100	0.096
Cu63	0.073	0.038	0.047	0.045		0.042	0.047
Zn66			0.072			0.133	0.072
As75	0.000	0.005	0.001	0.171			0.001
Ru99	0.107	0.104					0.105
Ru101	0.080	0.079					0.079
Rh103	0.018	0.018					0.018
Pd105	0.062	0.061					0.061
Pd106	0.050	0.050					0.050
Ag107			0.033	0.036			0.035
Cd111			0.079			0.243	0.079
Sn120	0.173	0.034	0.025	0.045		1.101	0.035
Te125				0.775			0.775
Re185	0.033	0.034				0.011	0.033
Os192	0.030	0.023	0.002				0.026
Ir193	0.024	0.022	0.016				0.023
Pt195	0.055	0.051	0.040			0.062	0.053
Au197	0.031	0.027	0.031	0.031			0.027
Pb208			0.015			0.026	0.015

Table 3.3 – Signal constraints

	cps/ppm	Detection Limit (ppb)
Ru101	342	30.6
Rh103	1225.1	71.9
Pd105	400.4	46.6
Pd106	492.6	14.6
Ag107	1309.3	104.9
Cd111	281.6	34.3
Sn120	1157.5	150.1
Te125	160.3	22.1
Re185	849.9	4.1
Os192	855.2	3.1
Ir193	1247.4	7.3
Pt195	504.4	14.9
Au197	1351.9	8.8
Pb208	1982.5	83.3

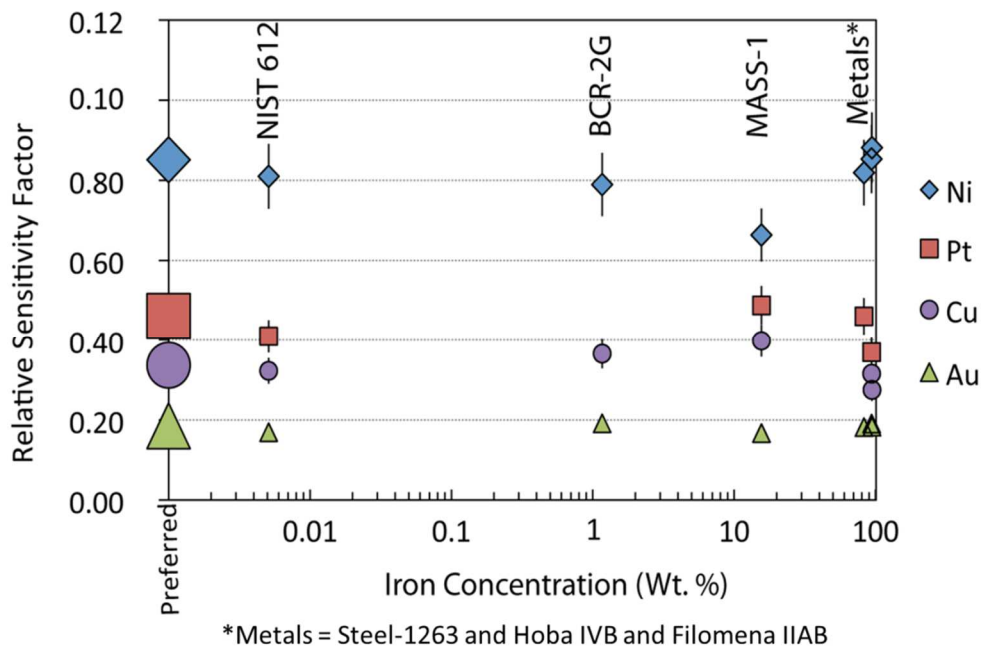


Figure 3.1 – The array of materials used for standardization, plotted as a function of Fe wt% and corresponding relative sensitivity factor (RSF). Standards include the glasses NISTSRM612 and BCR-2G, as well as a pressed-powder sulfide standard MASS-1, and metals that include Steel-1263 and the meteorites Hoba IVB and Filomena IIAB. Preferred RSFs are shown in larger symbols to the left of the figure. Error bars shown are 10% of the RSF. Note the general consistency of the RSF for a wide range of materials, both heavy and light elements, and Fe concentrations.

Chapter 4 Results

4.1 Bulk Rock Trace Elements

The trace element data demonstrate the depleted nature of these peridotites (Figure 4.1.1, Table 4.1.1). Low LREE/HREE ratios (La/Yb_N 0.001-0.27, N: PM-normalized), as well as low Ti and low Al concentrations (71.7-314.8 ppm and 1.0-2.5 wt%, respectively) suggest variable degrees of melt depletion and minimal refertilization, save for one sample (SE10-02) with flatter REE patterns (Fig. 4.1.1a). Low Sr and low U concentrations also indicate low water-rock ratios (Figure 4.1.1b), though strictly speaking, low Sr concentrations in peridotite are the result of an absence of carbonate phases (Kodolanyi et al., 2011). Sulfide S concentrations (Schwarzenbach et al., 2016), which range from 55-130 ppm, correlate positively with Ti concentrations, consistent with the incompatible nature of both elements during melting (Figure 4.1.2). This suggests that the bulk sulfide sulfur content must be largely primary and not alteration derived. The primary nature of the sulfide is confirmed by sulfur isotopic compositions for these samples, which are $< 2.5\%$ (Schwarzenbach et al., 2016). The high degree of melting determined based on Cr# from spinel (3-14%; Hellebrand et al., 2001; Cr# spinel data is from an unpublished Master's thesis of Shawn Write at the U. of Houston) is surprising considering the fact that there are still abundant sulfides remaining in the peridotites. Luquet et al. (2007) suggested that, depending on pressure during melting, BMS may be stripped from the system when partial melting exceeds 15%. This may explain why BMS are still present in these peridotites.

4.2 SEM Data

The primary sulfide phase observed in these peridotites is pentlandite, predominantly found interstitially in the serpentine matrix. While pure pentlandite is often observed (Figure 4.2.1a), other mineralogies are often also present within and around pentlandite grains. Magnetite often fills cleavage planes of pentlandites (Figure 4.2.1b,c). Bleb-like awaruite is also observed adjacent to pentlandite grains (Figure 4.2.1b). Some pentlandites are Cu-bearing, and some pentlandites are observed alongside native Cu blebs or Cu-sulfides such as covellite (Figure 4.2.1c,d). Only 4 sulfides were found that were included in a silicate phase, either orthopyroxene or clinopyroxene (Figure 4.2.1e). A few micron-sized PGE-rich alloys were also observed under SEM. PGE assemblages in such instances are typically some variation of Cu-Pt-Pd, Pt-Te, or Pt-Te-Au alloys (Figure 4.2.2). Such PGE alloys are observed adjacent to pentlandite, although the distance between the alloys and sulfides varies and some alloys are found within the matrix (Figure 4.2.2a vs. 4.2.2b).

4.3 Sulfide Major Elements

As the PGE (and other element) concentrations are calculated based on the Fe concentration of each sulfide derived by our LA-ICPMS method, the Fe data needs to be validated. I do so through a comparison between sulfide major elements calculated by our laser ablation method and electron microprobe data of sulfides from the same samples from Schwarzenbach et al. (2014; Figure 4.3.1). The two datasets show significant overlap. A slight deviation from the pentlandite field towards higher Fe concentrations in Figure 4.2.2 is attributed to inclusion of magnetite in laser ablation spot analyses due to the larger laser spot size compared to probe beam size. This deviation

from the pentlandite range is on the range of ~20% of the normalized Fe contribution to the sulfide composition. In contrast, PGE concentrations vary over orders of magnitude (discussed below). Any effect that Fe deviation would have on dilution of PGE signal is therefore much smaller relative to the variance of the PGE data.

LA-ICPMS derived major element data is shown on a sulfide classification diagram in Figure 4.3.2. Sulfides are color coded according to Cu concentration and magnetite inclusion. Sulfides shown in green to indicate high levels of magnetite included in the ablation beam were chosen based on their high Fe content (>49 wt%). Cu contents in sulfides are arbitrarily divided into two categories, intermediate Cu concentration (3 – 8 wt%) and high Cu concentration (>8 wt%). This color scheme is used in PGE concentration plots as well. Schwarzenbach et al. (2014) proposed that Cu-bearing mineral assemblages formed through interaction with a Cu-bearing hydrothermal fluid. Possible correlation between Cu concentration and PGE is thus observable with this color-coded Cu scheme.

4.4 Sulfide PGE Concentrations

PGE-Re concentrations in the St. Elena sulfides are highly variable, ranging from 1 – 100,000 times that of PM (Figure 4.4.1; Table 4.4.1). When describing PGE patterns, I may refer to IPGE and PPGE, which are defined as Ir-group PGE (Os, Ir, Ru, Rh) and Pt-group PGE (Pt, Pd, and the non-PGE Re), respectively. Most sulfides show approximately flat PM-normalized IPGE patterns with strong Pt depletions, lesser Pd depletions, and variably concentrated Re. Average sulfide concentrations are shown in Figure 4.4.1 as bold black lines for each sample. These average concentrations are

calculated as the sum of all sulfide concentrations, divided by the number of sulfides (Table 4.4.2 – nonfiltered average concentrations).

While average sulfide concentrations tend to have a relatively flat IPGE pattern, individual sulfides can have quite variable IPGE, especially between Os and Ir. Decoupling of Os and Ir from one another occurs systematically within some samples. Samples SE10-01 and SE10-16 have low average Ir/Os, while SE10-09 has high average Ir/Os (Figure 4.4.1). The reason for this decoupling in sulfides is not totally clear, and is discussed in more detail later. A plot of Os vs. Ir concentrations shows that our data does straddle a 1:1 line ($r^2 = 0.74$, $n = 114$), which is approximately chondritic. This suggests that overall and despite the occasional Os from Ir decoupling, Os and Ir do not fractionate from one another significantly over orders of magnitude, consistent with their similar compatibility in mantle sulfides (Palme and O'Neill, 2003; Becker et al., 2006; Cafagna and Jugo, 2015; Liu and Brenan, 2015). Ru in sulfides correlates well with both Os and Ir ($r^2 = 0.87$ and 0.9 , respectively). Rh is slightly elevated compared to other IPGE in some sulfides, though not all. Cu argide interferences may account for some of the Rh-rich sulfides, although no correlation was observed between Rh/Ir and Cu signals.

Pt and Pd vary by ~ 2 orders of magnitude more than IPGE (Figure 4.4.1). Pt is nearly ubiquitously depleted relative to IPGE by 3 orders of magnitude or more on a primitive mantle (PM) normalized plot (Figure 4.4.1). Pt enrichments (Pt_{PM} is greater than Ru_{PM} and Pd_{PM}) are observed in less than 10% of the ablated sulfides. Pd concentrations vary and are dominated by $Pd_{PM}/Os_{PM} < 1$, although $\sim 22\%$ of sulfides are enriched in Pd_{PM} relative to Ru_{PM} and Re_{PM} . Pd enriched sulfides are found in all samples. A weak positive correlation between Pd and Cu is observed (Figure 4.4.2). Re

concentrations typically vary more than IPGE but less than Pt and Pd. Re, though classically defined as having similar compatibility as Pt and Pd, does not correlate with either element.

4.5 Pt “Spikes” in Time Resolved Spectra

LA-ICPMS is a powerful tool for the detection of micron-sized phases located within sulfides. Time-resolved laser ablation spectra sometimes show very sharp and discrete transient Pt spikes, when IPGE spikes are absent (Figure 4.5.1). Figure 4.5.1a shows a Pt-enriched phase caught at the beginning of an ablation period, which is seen in conjunction with Te and Pd peaks. Figure 4.5.1b shows a sharp time-resolved Pt peak which coincides with a spike in Te. No Os, Ir, Ru, or Rh spikes are found in time-resolved spectra, though this does not exclude their presence.

4.6 Included Sulfides

Only 4 included sulfides were analyzed. A sulfide from SE10-19 was included in cpx, all other sulfides were held in opx. Included sulfide PGE patterns are very similar to interstitial sulfide patterns from the same sample, with similar PGE concentrations and strong Pt depletions (Figure 4.6.1). One included sulfide showed heterogeneity in Pt and Pd concentrations, though both elements remained depleted relative to IPGE. Pt and Pd in this cpx-included sulfide are variable by 3-4 orders of magnitude within ~30 μm .

4.7 Bulk Rock PGE

Bulk rock PGE patterns are relatively flat in a PM-normalized plot, with concentrations that straddle that of primitive mantle (Figure 4.7.1; Table 4.7.1). Concentrations relative to PM range from 0.40 to 2.0. Pt and Pd have the most variable

bulk rock concentrations. On average, Pd and Re are depleted relative to other PGE, with Re being more depleted than Pd. This slight depletion in Pd and Re is consistent with the small degrees of melting for these peridotites, as Pd and Re are the most incompatible of the plotted elements (Bockrath et al., 2004). Importantly, Pt is not depleted relative to IPGE in the bulk rock, unlike the in situ data above.

4.8 Bulk Rock Os Isotopic Composition

The $^{187}\text{Os}/^{188}\text{Os}$ signature of these peridotites is plotted in Figure 4.8.1 against measured bulk rock Re/Os concentrations (values reported in Table 4.8.1). Os isotopic signatures suggest a DMM origin for this suite of peridotites (Shirey and Walker, 1998). Re/Os in these samples falls below the typical DMM range, implying recent melt depletion (Shirey and Walker, 1998). A 130 Ma isochron is also plotted for reference as the age of cooling of the St. Elena ophiolite massif (Madrigal et al., 2015). St. Elena peridotites straddle this 130 Ma isochron, although they do not show any age information.

4.9 Chalcophile Element Concentrations

PGE patterns are color coded according to Cu content and shown in an extended pattern that includes the chalcophile elements Te, Au, and Pb (Figure 4.4.1). Chalcophile elements are shown in this way in an effort to better understand their variance with respect to PGE concentrations. Cu concentrations in the analyzed sulfides range from 253 ppm to 75.9 wt%. Te and Au concentrations range from 10 – 100,000 times that of PM. Some correlation is observed between Te, Au, and Pt (Figure 4.4.1, 4.9.1a). Te and Au concentrations do not correlate well with Cu (Figure 4.9.1a). Pb concentrations range

from 0.01 – 100 times PM; average Pb concentrations are 2.2 ppm. Pb does not correlate with any PGE or chalcophiles (Figure 4.9.1b).

Zn concentrations range from 0.1 ppm to 7.8 wt%; Zn does not correlate with any other measured element. Arsenic concentrations range from 0.1 – 45.5 ppm; As does not correlate with other elements. Ag concentrations range from 0.1 – 97.2 ppm. There is a strong positive correlation between Ag and Cu (save for one outlier with very low Ag and high Cu; Figure 4.9.1c). Cd concentrations range from 0.1 – 18.1 ppm; Cd does not correlate with any element. Sn concentrations range from 0.1 – 8.9 ppm; Sn does not correlate with other elements.

Table 4.1.1 – Bulk rock trace elements

	SE10-01	SE10-02	SE10-09	SE10-16	SE10-19
Li (ppm)	-0.45	0.12	-0.40	0.12	-0.21
Al (wt%)	1.55	2.40	1.02	2.41	2.50
Sc (ppm)	9.25	10.85	8.32	13.37	13.09
Ti	191.5	256.6	71.8	304.3	314.9
V	39.63	51.10	31.76	62.57	61.09
Cr	2131.3	2800.6	2232.7	2790.5	2495.7
Mn	797.1	944.2	811.8	845.1	950.7
Fe	51698.3	60204.0	52138.8	51776.2	58996.3
Co	90.41	103.16	92.98	87.92	98.23
Ni	1763.2	1942.5	1878.6	1672.0	1834.7
Cu	18.06	22.35	28.28	21.63	14.28
Zn	36.23	162.71	40.02	39.91	43.51
Ga	1.39	2.11	0.93	2.11	2.22
Rb	0.01	0.56	0.03	0.03	0.00
Sr	0.07	3.38	0.10	0.12	0.08
Y	1.29	1.29	0.38	2.07	1.79
Zr	0.33	0.62	0.07	0.33	0.36
Nb	0.00	0.02	0.00	0.00	0.00
Cd	0.01	0.04	0.01	0.01	0.01
Sn	0.01	0.46	0.02	0.01	0.02
Cs	0.00	0.01	0.00	0.00	0.00
Ba	0.00	1.59	0.01	0.09	0.02
La	0.00	0.07	0.00	0.00	0.00
Ce	0.01	0.05	0.00	0.01	0.01
Pr	0.01	0.03	0.00	0.01	0.01
Nd	0.07	0.17	0.01	0.08	0.08
Sm	0.06	0.07	0.01	0.08	0.07
Eu	0.03	0.03	0.00	0.04	0.04
Gd	0.12	0.11	0.02	0.18	0.16
Tb	0.03	0.02	0.01	0.04	0.04
Dy	0.21	0.19	0.05	0.33	0.28
Ho	0.05	0.05	0.01	0.08	0.07
Er	0.16	0.15	0.05	0.25	0.22
Tm	0.02	0.02	0.01	0.04	0.03
Yb	0.17	0.17	0.07	0.26	0.23
Lu	0.03	0.03	0.01	0.04	0.04
Hf	0.03	0.04	0.01	0.04	0.04
Ta	0.00	0.00	0.00	0.00	0.00
Pb	0.00	0.01	0.03	0.02	0.00
Th	0.00	0.00	0.00	0.00	0.00
U	0.00	0.00	0.00	0.00	0.00

Table 4.4.1 – Sulfide concentrations (bdl = below detection limit)

Sulfide	S (wt%)	Fe (wt%)	Ni (wt%)	Cu (wt%)	Co (wt%)	Mn (ppm)	Zn	As	Ru 99
SE10-01_S01a#	34.83	26.23	27.82	10.85	0.27	587	387	bdl	
SE10-01_S01c#	31.08	33.28	23.43	11.91	0.31	481	256	0.2	
SE10-01_S01d#	30.58	51.00	17.50	0.48	0.43	430	87	0.9	
SE10-01_S01a*	28.73	43.03	27.25	0.29	0.70	339	11	3.7	2.0
SE10-01_S01b*	29.04	45.17	24.92	0.12	0.75	371	8	3.7	14.0
SE10-01_S02\$	20.85	35.24	41.20	2.29	0.42	1199	21	bdl	
SE10-01B_IS01a*	33.81	36.28	26.09	3.09	0.74	343	6	4.7	19.8
SE10-01B_IS01b*	27.33	37.86	30.27	4.05	0.49	602	10	6.9	9.7
SE10-01B_S01*	29.04	41.30	27.04	2.25	0.37	322	31	5.5	42.4
SE10-01B_S02a*	33.86	42.13	22.21	1.38	0.42	99	26	4.2	148.4
SE10-01B_S02b*	29.96	47.04	20.67	2.00	0.33	237	30	5.3	88.0
SE10-01B_SC03a 1*	32.47	32.55	26.43	8.15	0.40	248	969	9.9	3.0
SE10-01B_SC03a 2*	26.01	44.00	24.11	5.34	0.55	520	8	9.5	16.3
SE10-01B_SC03a 3*	24.72	29.47	32.33	13.26	0.22	974	16	12.9	95.8
SE10-02_S02^	26.05	44.09	29.20	bdl	0.66	1451	51	bdl	
SE10-02_S02.5^	10.75	51.01	14.34	23.83	0.08	1666	332	bdl	
SE10-02_S02.7^	24.12	36.69	33.51	5.05	0.63	1821	113	bdl	
SE10-02_S0Z^	29.72	42.35	27.17	0.15	0.61	1069	7760	1.1	
SE10-02_S05^	29.15	31.50	30.37	8.38	0.60	321	24	bdl	
SE10-02_US1\$	24.17	54.23	19.76	1.40	0.44	625	12526	0.2	
SE10-02_US3a\$	30.01	35.56	22.78	11.20	0.45	1153	40	0.2	
SE10-02_US3b\$	26.77	15.47	18.86	38.40	0.50	1361	60	0.4	
SE10-02_S01a#	33.82	29.48	30.39	5.85	0.47	706	bdl	bdl	
SE10-02_S01b#	31.47	31.29	31.50	5.22	0.51	761	bdl	bdl	
SE10-02_S02b#	29.41	36.92	23.31	9.88	0.49	917	3621	2.2	
SE10-02_S03a#	40.00	31.30	27.50	0.69	0.51	1843	5741	3.6	
SE10-02_S03b#	28.72	39.01	31.05	0.58	0.63	1324	984	bdl	
SE10-02_S04#	8.24	12.37	8.89	70.37	0.13	849	bdl	4.0	
SE10-02_US01a#	28.36	33.91	36.91	0.20	0.62	16	bdl	0.5	
SE10-02_US01b#	29.76	31.98	36.39	1.32	0.55	1110	6	bdl	
SE10-02_US02a#	9.59	66.89	21.72	0.49	1.32	4851	28	14.9	
SE10-02_US02b#	45.96	28.50	25.01	0.06	0.47	945	20	bdl	
SE10-02_S03*	25.32	38.56	24.94	10.57	0.61	958	28	8.1	20.7
SE10-02_S01*	21.64	54.10	22.43	1.33	0.50	639	2300	3.7	19.3
SE10-02_S02*	30.05	43.30	25.88	0.08	0.69	910	15	3.0	32.1
SE10-02_S04*	32.54	47.06	17.76	2.45	0.20	14209	195	7.5	124.2

Ru 101	Rh	Pd 105	Pd 106	Ag	Cd	Sn	Te	Re	Os	Ir	Pt	Au	Pb
2.1	1.1	2.4	2.5	7.2	1.6	0.4	4.3	0.1	0.0	0.0	0.1	0.1	0.7
12.4	9.1	10.4	11.1	3.3	1.1	0.2	13.0	0.2	2.6	0.5	0.0	bdl	0.4
15.5	13.3	0.8	0.8	0.2	0.2	0.3	25.6	0.3	4.5	1.0	bdl	bdl	0.4
0.8	0.7	0.2	0.0	6.3	0.2	bdl	12.0	0.1	1.8	0.0	bdl	bdl	0.7
10.3	1.2	0.1	bdl	1.8	0.1	bdl	34.5	1.0	7.2	0.0	0.0	0.0	1.4
6.5	1.8	29.3	29.1	6.0	3.1	0.7	190.	0.8	33.3	22.6	115.	0.3	0.7
18.0	0.7	32.9	34.3	1.7	0.2	bdl	6.8	1.3	8.3	3.8	0.3	0.0	0.1
9.8	1.8	17.8	14.0	3.0	0.7	0.2	11.6	0.7	4.7	1.6	0.3	0.1	0.2
34.5	0.9	21.6	73.6	3.0	0.8	0.2	8.1	1.5	23.9	23.8	0.2	0.2	0.1
154.4	40.0	36.5	80.4	0.4	bdl	bdl	14.0	3.1	37.6	9.1	2.8	bdl	0.2
96.0	21.9	1.5	0.5	bdl	bdl	bdl	3.2	1.0	16.7	6.4	2.0	0.0	bdl
2.8	1.0	5.2	2.4	6.6	0.5	bdl	0.4	0.1	4.5	0.5	0.2	0.0	0.9
18.5	1.5	13.7	20.4	7.7	0.2	bdl	bdl	0.3	27.9	2.5	14.9	0.1	2.0
108.3	27.4	7.7	0.2	16.	0.3	bdl	16.7	1.2	33.2	14.5	0.2	bdl	0.3
50.3	27.8	0.1	0.1	bdl	4.2	0.2	22.0	1.9	17.1	15.2	0.0	bdl	0.1
0.9	0.7	1.1	1.1	15.	6.2	bdl	110.	bdl	0.3	2.7	20.7	0.0	0.2
26.5	5.6	9.6	9.6	5.5	6.9	0.4	3.5	0.9	8.8	10.5	6.4	0.0	0.2
3.3	0.3	0.1	0.3	1.4	5.0	bdl	5.8	0.2	1.0	0.6	bdl	0.0	1.1
1548.	238.	37.6	37.6	15.	3.7	bdl	9.9	1.6	805.	471.2	13.2	bdl	1.5
23.6	15.3	0.4	0.4	2.2	0.5	bdl	28.7	1.2	8.7	7.3	0.0	bdl	31.6
17.6	9.2	37.3	37.0	14.	1.6	0.3	66.2	1.1	3.0	2.3	3.0	bdl	0.4
1.1	2.5	39.2	38.9	4.7	2.8	bdl	6.2	bdl	0.0	0.0	0.7	bdl	0.1
77.0	7.7	130.	139.	5.0	0.8	bdl	0.1	1.7	48.1	30.8	0.0	bdl	0.1
89.6	8.7	122.	138.	4.2	0.4	0.2	0.5	2.1	50.5	31.9	1.5	0.1	0.2
82.2	37.1	0.1	0.1	19.	2.3	0.6	20.4	1.3	22.4	59.7	7.0	0.1	bdl
30.8	0.5	1.3	1.0	0.5	3.1	bdl	6.6	3.3	11.6	7.4	0.0	0.1	0.2
53.1	57.0	1.6	1.6	6.4	6.0	5.1	7179	5.3	25.8	60.3	902.	19.6	0.2
24.9	14.3	28.2	30.2	47.	0.9	bdl	58.2	2.0	14.1	10.9	bdl	0.1	0.1
115.8	26.7	0.5	bdl	0.9	0.4	bdl	14.6	3.3	48.5	41.7	5.5	0.1	0.2
223.3	18.6	55.8	59.6	2.6	3.5	bdl	66.2	6.0	89.0	48.5	9.4	bdl	0.1
25.1	7.5	10.6	18.2	1.0	11.	bdl	6.7	4.3	22.1	4.5	bdl	0.5	1.0
25.6	bdl	0.4	bdl	0.3	0.3	bdl	6.1	3.8	6.2	0.9	bdl	0.0	0.2
20.5	6.4	59.6	43.0	3.0	0.5	bdl	116.	2.8	7.9	6.4	3.1	0.1	bdl
21.0	6.6	0.7	0.1	0.7	1.5	bdl	35.3	1.5	6.4	3.3	bdl	bdl	bdl
29.9	0.8	0.1	bdl	2.7	0.1	bdl	14.7	1.9	14.1	22.9	0.0	bdl	bdl
130.5	48.5	0.7	bdl	12.	6.1	3.1	489.	3.8	29.3	22.2	0.6	bdl	2.1

Sulfide	S (wt%)	Fe (wt%)	Ni (wt%)	Cu (wt%)	Co (wt%)	Mn (ppm)	Zn	As	Ru 99	Ru 101
SE10-09_S01*	23.23	54.27	20.56	1.39	0.55	2586	87	6.3	2.0	1.0
SE10-09_S02*	6.79	11.75	5.44	75.95	0.08	236	337	37.7	1.2	0.6
SE10-09_S04\$	25.79	42.60	30.24	0.73	0.64	1774	138	0.1		14.9
SE10-09_S05\$	31.01	39.23	26.35	2.37	1.04	3739	849	0.9		68.7
SE10-09_S01#	24.68	57.57	15.42	1.82	0.51	1136	33	1.7		46.8
SE10-09_S02a#	34.13	37.74	22.10	5.82	0.22	621	7810	5.6		69.7
SE10-09_S02b#	33.85	47.87	17.81	0.30	0.18	1407	446	5.0		210.
SE10-09_S0Za#	43.99	24.03	29.58	1.78	0.63	3073	479	3.1		26.8
SE10-09_S0Zb#	24.57	50.73	23.59	0.05	1.06	598	1984	bdl		23.7
SE10-09B_S01a*	11.71	57.19	30.26	0.29	0.55	749	19	3.2	16.4	11.3
SE10-09B_S01b*	24.85	55.95	18.69	0.16	0.36	3798	55	2.7	7.5	8.3
SE10-09B_S01c*	26.94	48.69	23.74	0.24	0.38	1133	1605	3.3	17.1	20.2
SE10-09B_S01d*	30.39	44.46	24.39	0.29	0.46	1063	252	3.8	54.3	52.1
SE10-16_S01\$	32.63	38.89	26.15	1.82	0.52	759	626	0.1		7.1
SE10-16_S03b\$	26.57	48.63	24.18	0.03	0.59	1780	86	1.0		40.6
SE10-16_S03a\$	27.96	34.93	31.85	4.67	0.59	4013	99	0.6		38.4
SE10-16_S04\$	36.81	43.01	19.40	0.29	0.48	1473	46016	6.2		3149
SE10-16_S04#	32.66	35.17	31.37	0.22	0.58	2652	2159	1.9		149.
SE10-16_US0Y#	28.43	42.84	27.09	1.14	0.50	219	986	1.2		16.1
SE10-16_US01#	25.69	42.40	31.19	0.16	0.56	1490	2751	bdl		5.5
SE10-16_US02a#	28.93	40.46	24.53	5.68	0.40	263	3131	bdl		10.5
SE10-16_US02b#	29.67	42.83	21.46	5.63	0.40	230	1713	bdl		5.6
SE10-16_US02c#	26.27	45.38	26.21	1.59	0.56	153	1036	bdl		107.
SE10-16_S01a#	17.67	50.80	26.29	4.68	0.56	816	52610	bdl		139.
SE10-16_S01b#	35.10	44.44	18.37	1.56	0.54	2828	74806	8.7		17.3
SE10-16_S0Xa*	16.94	61.28	20.71	0.47	0.60	3399	578	2.6	9.1	7.6
SE10-16_S0Xb*	24.47	47.74	26.57	0.43	0.80	2797	198	4.1	50.9	49.9
SE10-16_S04a*	29.29	50.16	19.88	0.10	0.57	1504	132	2.2	8.9	11.0
SE10-16_S04b*	28.74	66.82	2.98	1.31	0.15	15669	156	3.3	63.8	314.
SE10-16_S03*	20.68	50.69	27.20	0.76	0.67	886	18	3.6	10.4	11.2
SE10-16_S02a*	35.03	39.53	23.81	1.18	0.44	1023	10	4.3	52.8	82.4
SE10-16_S02c*	18.32	36.83	22.26	21.75	0.84	1022	15141	19.2	10.3	15.6
SE10-16_S01a*	27.52	41.93	24.05	5.83	0.67	1669	1430	10.4	35.9	38.3
SE10-16_S01a*	6.82	82.75	3.71	6.61	0.10	18427	401	6.6	bdl	1.0
SE10-16_S01b*	42.93	6.00	27.54	22.89	0.64	11260	202	35.9	28.5	13.9
SE10-16_S01c*	26.55	34.43	18.38	20.17	0.47	940	9	12.0	30.5	25.3

Rh	Pd105	Pd106	Ag	Cd	Sn	Te	Re	Os	Ir	Pt	Au	Pb
0.6	2.4	1.4	3.5	2.3	bdl	90.0	3.7	3.0	3.3	1.4	3.6	5.6
45.7	928.3	953.7	97.2	3.7	0.4	57.7	0.0	1.2	1.0	125.7	0.6	0.1
5.0	18.8	18.6	1.1	1.1	bdl	19.5	0.7	6.3	6.7	bdl	0.0	0.6
10.4	23.1	22.9	2.4	4.7	0.3	87.7	3.4	33.0	28.4	1.2	0.5	3.3
9.9	27.3	29.2	11.9	7.3	0.6	126.1	2.9	25.2	15.8	3.2	0.1	1.5
12.7	1.6	1.2	1.9	5.6	0.6	53.1	3.4	25.9	51.2	bdl	bdl	1.8
8.9	3.8	bdl	0.8	0.4	0.7	117.2	8.9	41.7	17.9	4.5	0.2	0.9
687.3	99.2	105.9	8.3	2.9	bdl	2508.2	11.4	14.2	67.2	548.8	bdl	2.8
2.8	bdl	0.0	0.9	0.4	bdl	23.0	1.1	17.5	13.4	bdl	bdl	0.3
86.4	0.1	0.1	1.4	0.9	bdl	2.7	0.7	3.6	59.7	0.2	bdl	2.2
52.6	0.1	bdl	2.2	0.8	0.2	4.8	0.2	0.7	39.5	0.1	bdl	0.9
20.3	0.1	0.0	2.1	0.8	bdl	3.5	0.4	4.4	24.2	bdl	0.0	4.9
1.3	0.2	0.2	3.4	1.9	bdl	9.1	0.7	10.8	64.9	0.1	bdl	13.1
0.9	3.1	3.0	3.0	1.7	bdl	3.1	0.5	4.8	3.8	2.4	0.1	0.6
10.2	6.5	6.5	1.2	0.7	bdl	28.8	2.5	20.7	16.6	bdl	bdl	2.3
10.1	0.9	0.9	2.1	0.2	0.4	17.0	2.4	20.5	16.5	0.1	bdl	2.9
132.6	17.8	18.8	2.0	6.4	0.2	51.1	2.2	838.9	1885.5	102.3	0.3	2.4
37.3	1.5	2.3	3.4	0.5	0.7	173.8	8.2	44.3	46.9	58.9	bdl	1.8
7.8	0.2	0.1	2.4	0.8	bdl	19.4	0.6	4.2	4.2	bdl	bdl	4.5
0.1	1.0	0.9	1.1	4.0	bdl	1.4	bdl	6.2	1.3	0.1	0.0	31.4
0.6	0.1	0.2	19.2	1.0	0.2	bdl	0.1	8.1	0.4	0.0	bdl	13.7
2.7	0.4	0.3	13.9	0.5	bdl	0.8	0.1	3.7	0.8	0.4	bdl	16.6
29.5	0.3	0.3	6.0	0.4	0.2	8.7	0.6	33.9	5.7	bdl	bdl	1.5
63.0	1.7	1.8	2.2	1.5	0.3	32.8	2.5	109.0	76.1	28.4	bdl	0.2
2.3	6.3	9.1	0.7	10.0	1.7	49.6	69.5	15.0	5.7	644.3	bdl	1.1
0.3	0.3	0.4	1.1	2.5	bdl	bdl	0.8	8.4	4.4	0.1	0.1	1.5
0.2	5.3	4.2	3.2	1.1	bdl	11.0	1.3	35.6	21.7	2.3	bdl	0.3
11.8	0.1	0.4	2.1	13.2	bdl	2.6	0.8	8.5	10.5	37.1	0.1	14.1
39.4	1554.5	296.0	8.0	bdl	8.9	143.8	6.4	25.1	7.6	83.1	0.5	6.0
0.6	0.5	0.1	2.3	0.2	bdl	6.6	1.0	8.3	1.4	0.0	bdl	3.7
12.7	1.3	0.2	0.8	0.1	bdl	37.8	3.5	21.0	15.1	bdl	0.0	0.3
5.5	40.5	23.9	4.2	10.4	bdl	16.7	2.6	18.0	9.1	0.1	0.5	1.5
1.8	39.2	29.6	8.0	0.7	bdl	26.9	1.1	17.9	15.4	bdl	0.0	bdl
0.7	4.2	4.1	3.1	2.1	0.8	6.8	0.0	0.1	0.0	bdl	140.4	0.4
3.8	76.7	43.3	bdl	1.3	6.2	bdl	0.2	10.8	19.7	1.2	bdl	0.9
2.1	13.3	0.6	4.9	1.1	bdl	8.8	1.6	27.9	18.0	2.8	0.1	bdl

Sulfide	S (wt%)	Fe (wt%)	Ni (wt%)	Cu (wt%)	Co (wt%)	Mn (ppm)	Zn	As	Ru 99
SE10-19_S07a^	23.63	56.27	18.91	0.86	0.33	525	22	bdl	
SE10-19_S07b^	25.59	54.04	19.62	0.41	0.34	631	18	bdl	
SE10-19_S0Za^	28.05	49.15	21.49	0.94	0.38	1002	10361	0.9	
SE10-19_S0Zb^	21.80	57.21	19.97	0.64	0.38	991	1665	bdl	
SE10-19_S03^	17.59	65.85	14.96	1.26	0.34	1324	10455	1.1	
SE10-19_S03M^	10.26	80.73	8.57	0.21	0.23	1272	216	bdl	
SE10-19_S02^	24.79	56.49	17.75	0.55	0.43	474	3858	bdl	
SE10-19_S02b^	25.37	49.76	21.69	2.84	0.34	593	9083	bdl	
SE10-19_S01^	28.36	48.38	21.84	1.03	0.38	823	10937	0.4	
SE10-19_S01b^	21.53	56.85	20.74	0.50	0.39	780	1043	1.4	
SE10-19_S02a#	34.15	37.14	25.61	2.64	0.46	374	19	bdl	
SE10-19_S03b#	30.04	48.50	20.56	0.51	0.39	638	13	bdl	
SE10-19_S04a#	33.06	33.09	30.25	3.22	0.38	1108	33	bdl	
SE10-19_S04b#	36.13	33.10	28.49	1.84	0.44	143	3	0.6	
SE10-19_S04c#	32.77	23.65	29.01	14.23	0.33	118	921	0.9	
SE10-19_S05b#	36.68	35.77	26.92	0.03	0.61	79	172	bdl	
SE10-19_S06b#	5.13	87.01	7.37	0.15	0.33	898	1981	45.5	
SE10-19_S0Z#	26.80	47.35	24.92	0.60	0.33	429	84	1.7	
SE10-19_S01a#	11.94	73.52	13.91	0.03	0.59	2810	4260	1.6	
SE10-19_S01b#	15.38	68.39	13.81	1.85	0.56	1492	24738	0.8	
SE10-19_S07a#	60.06	25.91	12.83	0.95	0.24	119	685	4.9	
SE10-19_S07b#	26.39	51.42	21.55	0.23	0.41	982	1318	bdl	
SE10-19_S08a#	14.28	55.84	29.02	0.57	0.28	500	457	bdl	
SE10-19_S08b#	48.96	26.45	24.04	0.33	0.22	711	543	bdl	
SE10-19_SC05a*	14.21	26.48	44.06	12.50	2.76	5170	35	31.1	13.4
SE10-19_SC05b*	17.40	74.40	5.80	2.04	0.35	19040	111	1.6	11.3
SE10-19_SC03a*	19.85	44.15	32.83	2.83	0.33	2952	5115	9.4	24.0
SE10-19_SC03b*	18.61	60.41	20.24	0.26	0.48	3290	1886	3.6	17.1
SE10-19_SC03c*	24.27	49.04	16.80	9.52	0.37	1490	53116	17.7	20.9
SE10-19_SC03d*	28.17	50.81	20.43	0.12	0.47	518	17020	10.1	32.8
SE10-19_ISC04a*	28.11	37.93	31.38	1.90	0.68	666	65	6.7	11.0
SE10-19_ISC04b*	25.93	40.29	32.37	0.90	0.50	447	680	5.7	67.0
SE10-19_S0Y*	16.86	59.35	22.53	0.62	0.64	2400	22026	10.7	4.1
SE10-19_S09b 1*	32.01	45.35	20.97	1.29	0.38	592	2095	5.8	2.3
SE10-19_S09b 2*	30.86	40.85	26.92	0.93	0.44	384	3715	5.8	4.5
SE10-19_S09a*	30.15	37.74	31.20	0.42	0.48	409	563	4.3	11.2
SE10-19_IS08a opx*	17.61	39.80	35.70	6.35	0.54	3346	2455	14.8	0.7
SE10-19_IS08b opx*	41.82	16.88	30.60	10.33	0.37	4837	4471	15.7	2.6
SE10-19_S10*	21.17	44.13	27.49	6.41	0.80	2035	57592	24.2	17.4
SE10-19_SC07a 1*	21.63	2.93	74.33	0.81	0.30	1190	1830	28.4	445.2
SE10-19_SC07a 2*	27.74	40.92	24.20	6.88	0.26	3422	45	10.9	17.7
SE10-19_SC07a 3*	24.55	50.30	23.25	1.48	0.41	2464	219	6.3	42.0

Ru 101	Rh	Pd 105	Pd 106	Ag	Cd	Sn	Te	Re	Os	Ir	Pt	Au	Pb
1.1	0.5	bdl	0.0	2.1	0.8	bdl	0.8	0.3	4.1	1.6	0.0	bdl	3.1
1.2	0.6	0.2	bdl	1.6	0.6	bdl	0.1	0.2	3.7	1.4	bdl	0.0	2.3
11.6	2.2	0.2	0.2	2.2	2.2	0.7	0.4	0.5	19.2	11.0	0.0	bdl	0.8
53.4	12.4	bdl	0.0	1.4	0.7	bdl	3.9	1.3	26.0	30.9	bdl	bdl	0.2
35.9	6.6	0.4	0.1	2.8	3.5	bdl	2.4	0.9	8.4	20.4	bdl	bdl	3.5
47.6	8.3	0.2	bdl	0.6	2.3	0.2	6.5	0.7	22.0	23.3	bdl	bdl	2.3
27.1	3.5	bdl	0.0	0.3	0.2	bdl	2.9	1.0	14.2	16.4	bdl	bdl	0.5
46.9	4.6	0.1	0.1	1.0	1.1	bdl	6.7	1.4	23.6	19.0	bdl	0.0	2.1
11.9	2.2	0.1	0.1	2.4	1.7	0.3	0.4	0.5	20.0	11.2	0.0	bdl	0.7
55.8	12.7	bdl	0.0	1.1	0.5	0.2	4.1	1.4	28.8	34.0	0.0	bdl	0.1
2.0	2.9	0.1	0.1	3.8	0.8	bdl	8.0	0.0	2.7	0.4	0.1	0.0	1.7
4.8	3.1	0.2	0.2	2.1	1.8	bdl	2.3	0.7	2.6	6.5	bdl	0.0	1.9
7.1	18.8	0.2	0.2	9.6	1.9	bdl	9.2	0.8	3.1	16.4	bdl	bdl	dbl
22.7	13.4	bdl	bdl	0.5	0.6	bdl	14.2	1.4	11.6	8.3	bdl	bdl	bdl
23.4	10.7	4.3	4.6	4.9	5.1	bdl	30.1	1.0	8.2	6.1	0.0	0.0	0.1
3.4	0.4	bdl	0.1	1.0	0.7	bdl	8.7	0.2	1.3	0.9	bdl	bdl	bdl
1.1	5.8	0.9	1.0	0.6	3.6	bdl	0.7	0.4	3.4	5.0	0.1	0.0	1.4
18.8	2.9	1.2	1.3	0.8	1.1	bdl	27.3	0.9	8.8	7.3	bdl	0.0	1.8
192.4	14.8	0.1	0.7	0.5	8.5	bdl	19.1	2.8	68.6	21.8	bdl	bdl	0.4
24.7	5.2	3.9	bdl	1.8	11.2	0.5	bdl	0.4	30.0	36.4	1.0	bdl	0.1
734.9	2.0	1.5	1.6	2.7	1.4	0.2	16.4	3.4	125.6	77.6	bdl	bdl	6.0
202.9	1.7	0.4	0.3	0.9	3.0	bdl	10.1	1.7	47.5	22.0	bdl	bdl	5.6
22.3	12.7	1.4	1.8	2.7	2.2	1.0	10.5	2.3	15.7	38.8	bdl	bdl	1.3
22.5	8.2	0.1	bdl	0.2	2.6	bdl	4.1	0.3	24.8	16.3	bdl	bdl	0.2
3.8	6.3	27.4	22.1	5.3	15.0	2.7	6.0	1.6	22.8	30.5	13.8	0.8	0.9
0.1	1.9	1.6	4.1	18.4	bdl	bdl	28.3	bdl	2.0	14.4	3.1	2.7	dbl
22.5	2.9	3.7	1.8	1.5	1.1	3.1	23.8	1.3	13.3	1.8	bdl	0.1	0.6
22.4	0.2	0.2	0.1	0.8	0.1	0.2	1.9	1.3	4.3	1.7	0.1	bdl	0.1
17.6	6.8	63.2	52.8	30.1	10.6	0.4	135.0	0.6	2.9	2.4	24.6	15.1	0.5
29.7	5.6	1.7	1.5	2.4	3.9	0.2	30.3	1.7	6.8	3.0	0.0	0.0	0.1
11.4	4.9	1.0	bdl	1.7	0.3	bdl	7.6	0.9	10.0	11.4	bdl	bdl	0.4
63.1	11.3	3.0	3.2	1.1	2.3	bdl	41.6	2.6	33.7	20.4	4.3	bdl	1.1
2.8	2.1	0.4	0.6	0.5	3.9	bdl	24.6	1.4	2.9	6.7	0.0	bdl	0.1
2.3	bdl	0.4	0.1	0.5	0.8	bdl	5.0	0.3	1.8	2.0	bdl	bdl	0.2
4.3	2.2	0.6	0.1	0.9	1.8	bdl	27.0	0.6	3.0	6.1	0.0	0.1	0.1
9.7	7.4	0.2	bdl	0.8	0.7	0.1	6.5	0.8	11.8	17.7	0.0	bdl	0.2
0.3	2.4	316.4	98.2	11.4	10.3	0.7	2.6	0.1	0.8	2.8	13.7	bdl	7.5
2.7	7.4	119.4	124.5	68.2	12.2	5.6	8.2	0.1	0.3	5.1	11.9	bdl	0.9
15.6	4.9	3.7	0.4	12.0	18.1	0.4	59.9	0.8	2.2	1.0	0.0	bdl	0.3
158.4	1.5	bdl	0.3	2.3	6.7	bdl	316.2	3.8	209.8	261.1	bdl	0.0	2.0
15.6	4.5	1.7	8.1	17.8	1.6	1.9	243.1	1.0	10.7	10.6	26.4	0.9	0.9
38.2	2.3	1.7	0.7	53.0	1.6	bdl	20.8	1.1	17.6	5.8	1.7	0.1	1.4

Table 4.4.2 – Average PGE sample concentrations (ppm)

Non-filtered average concentrations													
Sample	Ru101	Rh	Pd106	Ag	Cd	Sn	Te	Re	Os	Ir	Pt	Au	Pb
SE10-01	35.0	8.8	19.2	4.5	0.6	0.2	24.3	0.8	14.7	6.2	9.8	0.1	0.6
SE10-02	119.1	24.5	25.2	7.6	3.1	0.4	375.8	2.3	56.4	39.1	44.3	0.9	1.8
SE10-09	42.7	72.6	87.1	10.5	2.5	0.2	238.7	2.9	14.4	30.3	52.7	0.3	2.9
SE10-16	185.1	16.3	19.4	4.1	2.3	0.8	27.1	4.7	56.1	95.1	41.9	6.1	4.7
SE10-19	47.5	5.5	7.9	6.6	3.5	0.4	28.0	1.0	21.0	19.9	2.4	0.5	1.2
Filtered average concentrations													
Sample	Ru101	Rh	Pd106	Ag	Cd	Sn	Te	Re	Os	Ir	Pt	Au	Pb
SE10-01	37.5	10.1	22.4	4.6	0.7	0.2	24.5	0.9	16.4	7.2	11.4	0.1	0.5
SE10-02	53.2	12.8	25.1	7.4	2.9	0.2	56.5	2.3	21.5	17.4	3.0	0.0	2.0
SE10-09	47.6	19.2	6.7	2.9	2.4	0.2	48.8	2.4	15.7	29.6	1.0	0.4	3.2
SE10-16	38.2	11.4	20.3	4.3	1.7	0.7	26.9	1.8	20.8	14.1	10.3	0.0	5.3
SE10-19	46.3	5.6	7.7	7.1	3.6	0.3	29.6	1.0	20.5	19.5	2.3	0.4	1.2

Table 4.7.1 – Measured bulk rock & reconstructed PGE concentrations

Bulk Rock PGE concentrations									
Sample	Os	Ir	Ru	Pt	Pd	Re			
SE 10-01	5.681	5.016	8.880	10.173	8.545	0.225			
SE 10-02	4.185	4.514	6.746	7.817	4.748	0.140			
SE 10-09	7.502	6.236	11.949	14.971	14.240	0.454			
SE 10-16	3.716	3.116	6.161	6.433	7.341	0.315			
SE 10-19	3.909	3.564	6.340	7.654	4.021	0.181			
Filtered Reconstructed Bulk									
Sample	Os	Ir	Ru	Pt	Pd	Re			
SE 10-01	6.18	2.71	14.10	4.28	8.44	0.33			
SE 10-02	12.20	9.84	21.40	1.70	14.24	1.29			
SE 10-09	2.61	4.93	7.93	0.16	1.11	0.40			
SE 10-16	8.12	5.49	14.90	4.03	7.91	0.72			
SE 10-19	7.62	7.26	17.25	0.86	2.87	0.38			
Non-filtered Reconstructed Bulk									
Sample	Os	Ir	Ru	Pt	Pd	Re	Te	Au	Pb
SE 10-01	5.54	2.32	12.39	3.67	7.23	0.31	9.13	0.02	0.22
SE 10-02	31.95	22.19	67.32	25.08	14.31	1.29	213.02	0.53	1.03
SE 10-09	2.40	5.04	7.06	8.79	14.53	0.48	39.79	0.06	0.49
SE 10-16	21.90	37.09	67.26	16.34	7.58	1.84	10.56	2.39	1.83
SE 10-19	7.80	7.42	17.63	0.89	2.93	0.39	10.43	0.17	0.44

Table 4.8.1 – Bulk Os isotopic composition

Sample	187/188Os	±2s
SE 10-01	0.12333	0.0001
SE 10-02	0.12336	0.00012
SE 10-09	0.12349	0.0002
SE 10-16	0.12595	0.00013
SE 10-19	0.12558	0.00013

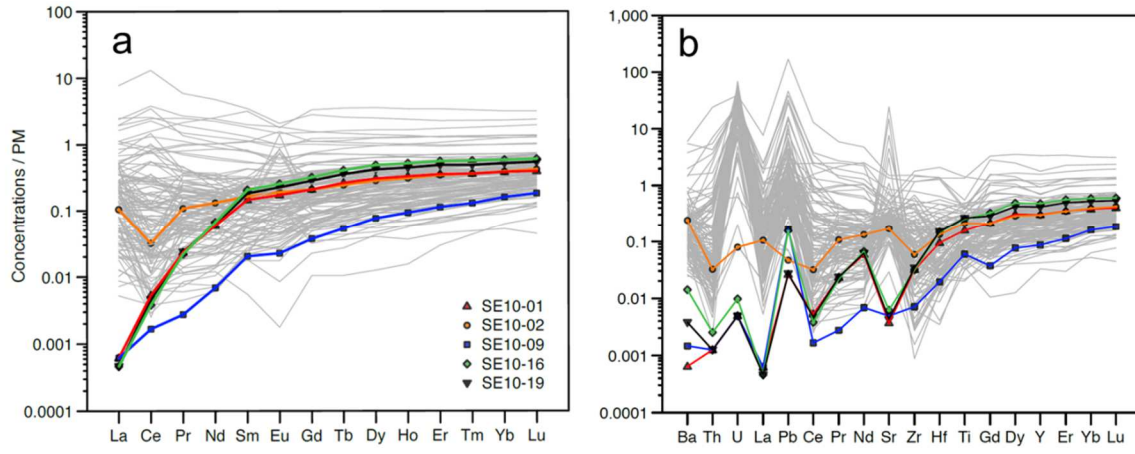


Figure 4.1.1 – a) Rare earth element (REE) and b) extended trace element bulk rock data of the St. Elena peridotites normalized to Primitive Mantle (PM). Global abyssal peridotite data is shown in grey (Niu, 2004). St. Elena peridotites overlap the global range of abyssal peridotite REE concentrations but also have much lower U, Ba, Th, La, and Sr, likely suggesting less refertilization and less reaction with seawater.

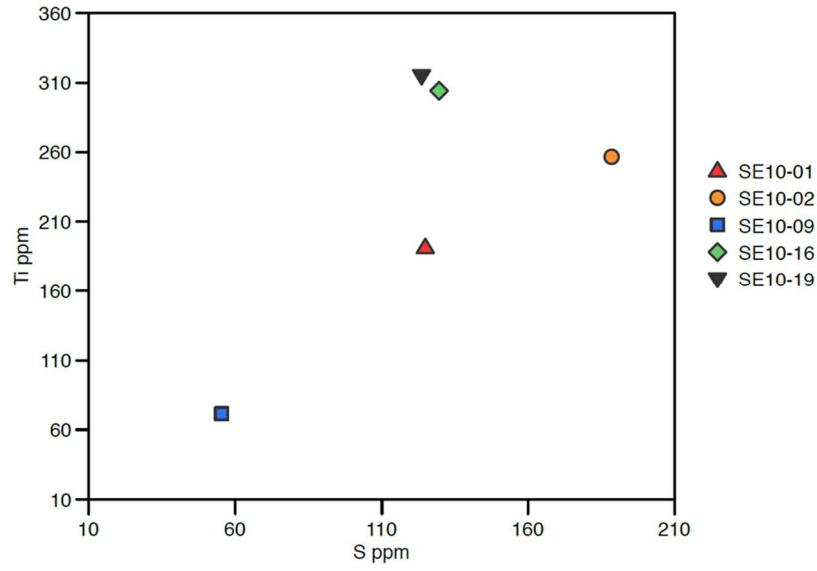


Figure 4.1.2 – Bulk rock sulfide sulfur concentrations vs. Ti concentrations, in ppm. Note the roughly positive trend. Sulfide S concentrations are reported in Schwarzenbach et al. (2016).

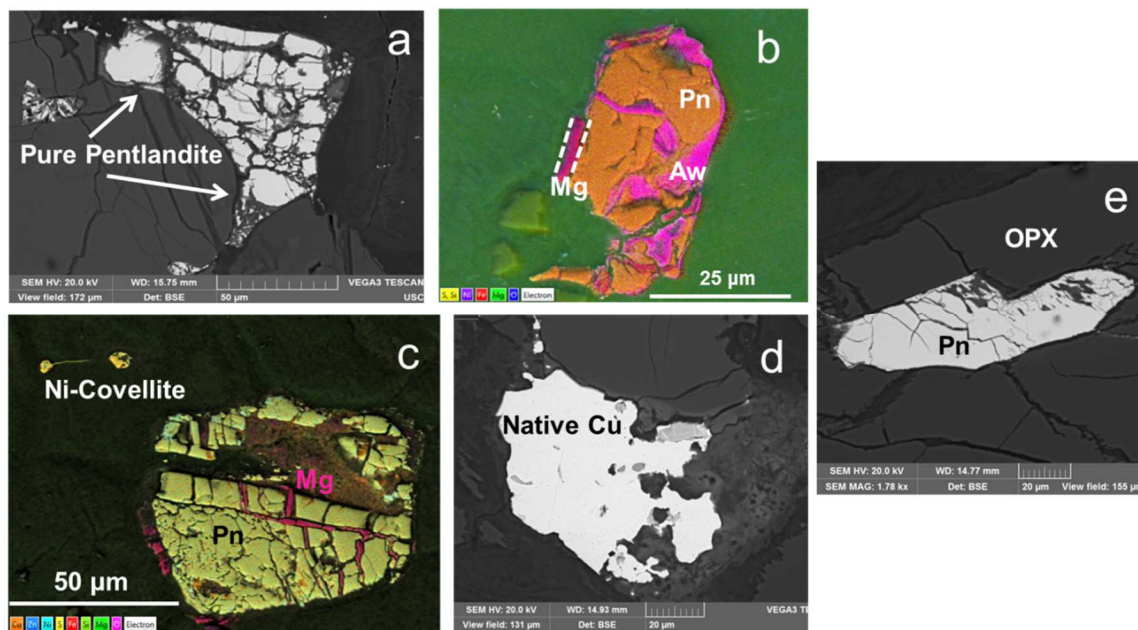


Figure 4.2.1 – Back-scattered electron (BSE) images and compositional images of typical ablated sulfides in a-d) a serpentine matrix and e) orthopyroxene. A) Pentlandite (Pn) with no impurities; b) pentlandite with magnetite (Mg) and bleb-like awaruite (Aw; $\text{Ni}_2\text{-}_3\text{Fe}$); c) pentlandite with magnetite filling cleavage planes, and two blebs of Ni-covellite $\sim 25 \mu\text{m}$ away from the pentlandite; d) $\sim 50 \mu\text{m}$ native Cu bleb found in SE10-09; e) pentlandite grain with an absence of other mineralogies included within an orthopyroxene (opx) grain.

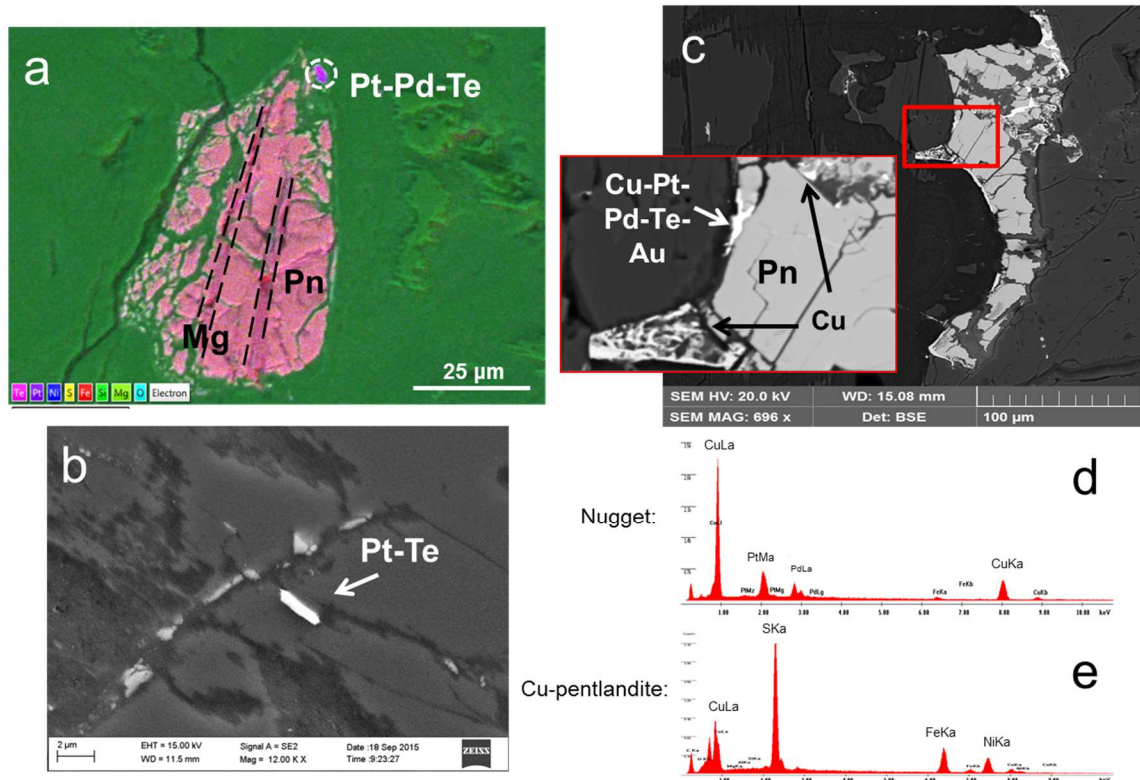


Figure 4.2.2 – BSE images of ablated phases which include Pt nuggets. a) Pt-Pd-Te nugget no more than 5-10 μm distant from a pentlandite grain with magnetite. b) Pt-Te nugget which is $\sim 10 \mu\text{m}$ from a pentlandite grain outside the field of view. c) A Cu-Pt-Pd-Te-Au nugget abutting a pentlandite grain with native Cu phases filling fractures in the pentlandite. The EDS spectra for the Cu-Pt-Pd nugget are shown in d) and the pentlandite shown in e). High Te-Au concentrations in the Cu-Pt-Pd nugget were found in LA-ICPMS spectra, not in the EDS spectra.

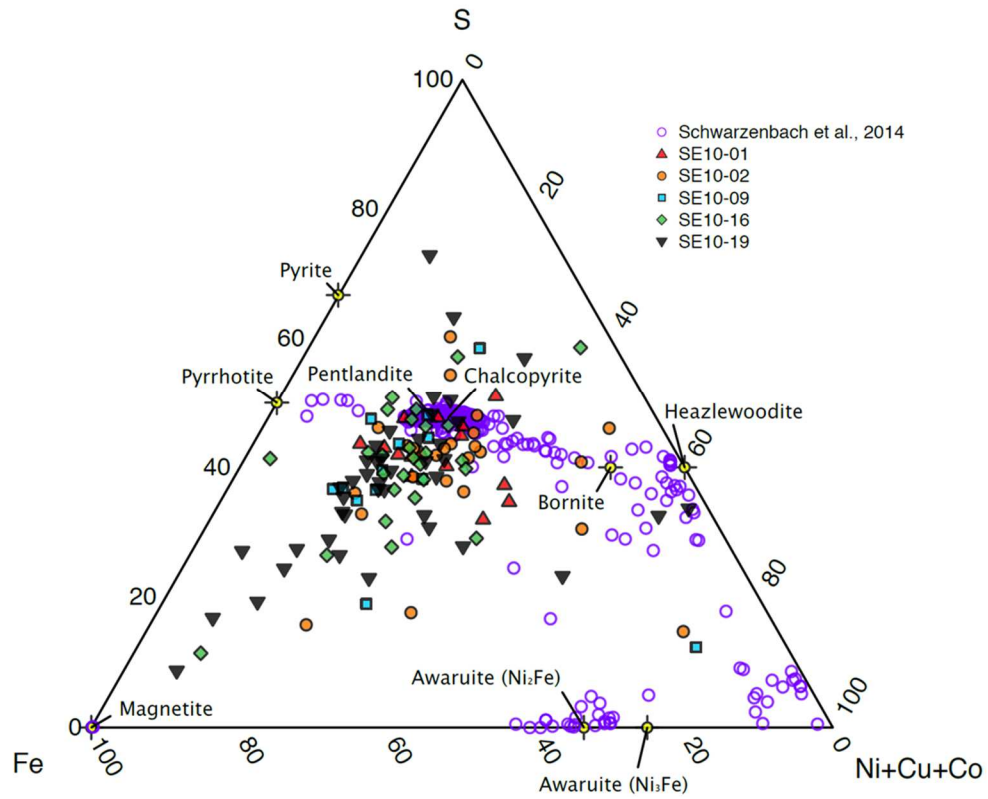


Figure 4.3.1 – Sulfide classification diagram (atom %) comparing microprobe data from Schwarzenbach et al. (2014) and LA-ICPMS data from this study. Data is color-coded by sample. Microprobe analyses were performed at 1 μm ; LA-ICPMS analyses were done at 10 μm or greater.

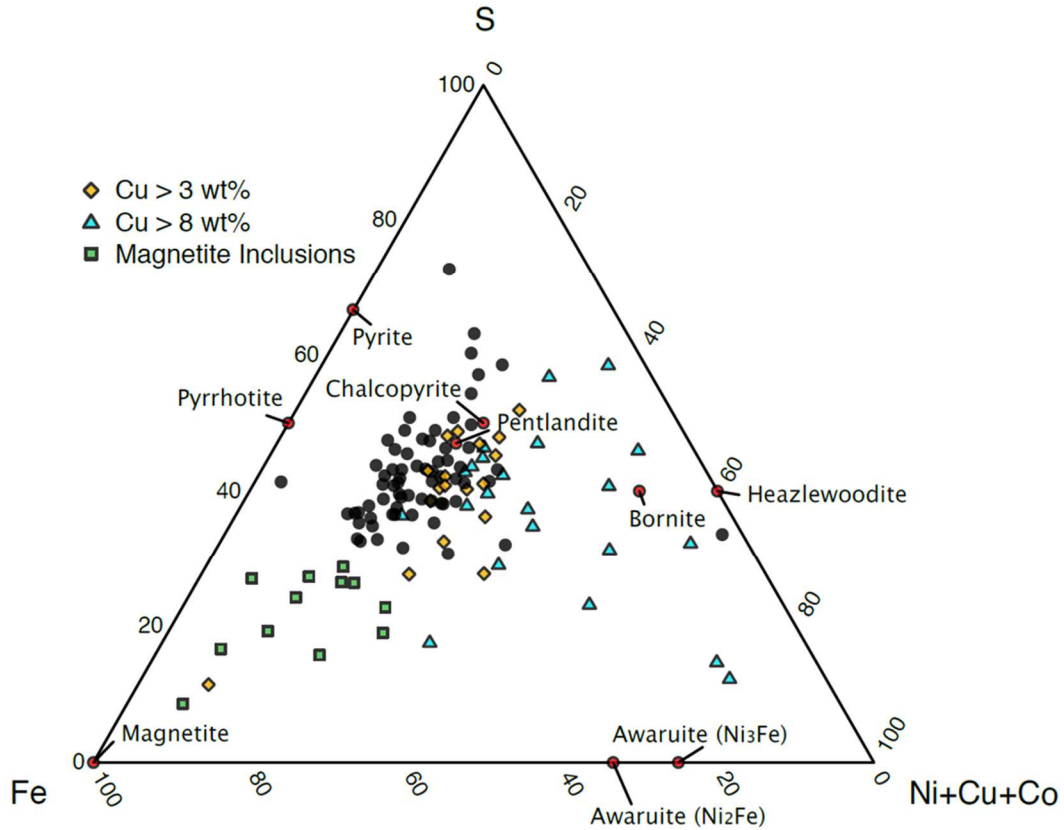


Figure 4.3.2 – Sulfide classification diagram (atom %) from this study (LA-ICPMS data). Data as in Figure 6. Range in compositions towards the Fe apex is due to the low spatial resolution of LA-ICPMS relative to the scale of heterogeneity in the sulfides. The majority of sulfides plot in the pentlandite range, with mixing towards magnetite, heazlewoodite, and native Cu. Sulfides were ablated at 10 μm or greater. Sulfides are color coded according to Cu concentrations and magnetite inclusions. The compositions of different mineralogical phases are shown for reference.

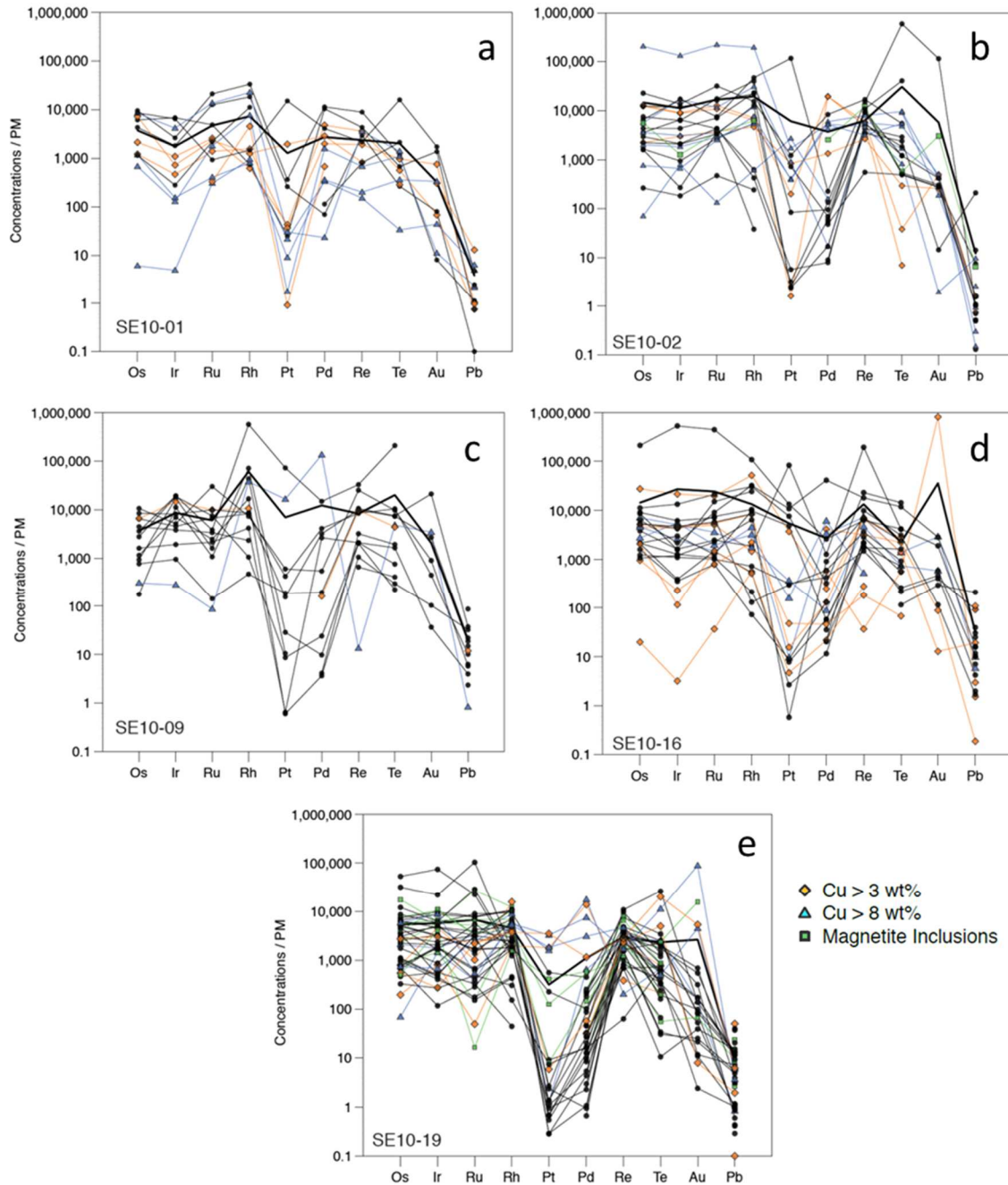


Figure 4.4.1 – Sulfide PGE concentrations normalized to primitive mantle (PM). Individual sulfides have highly variable concentrations within each sample. Average sulfide concentrations are shown in bold. Sulfides are color coded as in Figure 6, based on Cu and magnetite inclusions. Error bars are smaller than symbol size. PM concentrations of Os, Ir, Ru, Pt, Pd, Re from Becker et al. (2006); Rh and Au from Godde et al. (2011); Te and Pb from McDonough and Sun (1995).

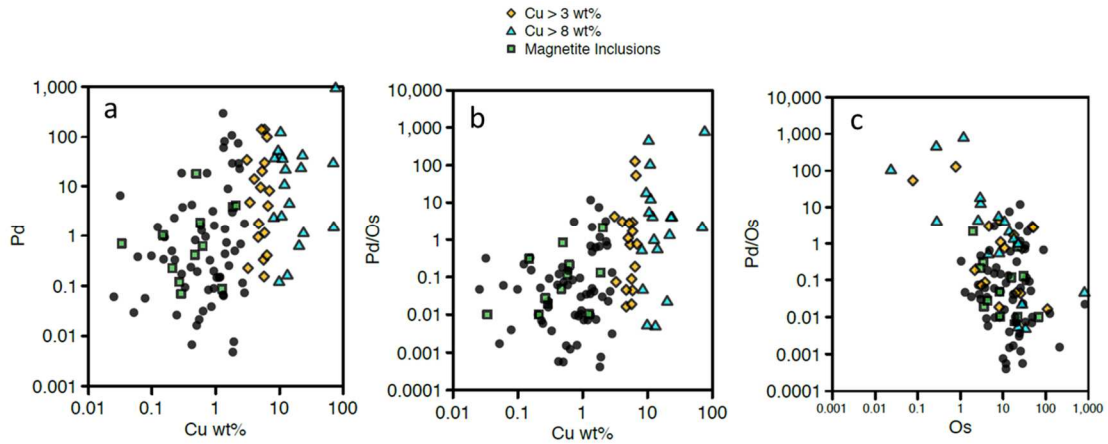


Figure 4.4.2 – Comparisons of Pd, Os, and Cu concentrations of individual sulfides. a) Pd (ppm) versus Cu (wt%) concentrations show no direct correlation. b) Pd/Os versus Cu concentrations show a positive correlation, implying a link between PGE systematics and Cu. c) Pd/Os versus Os (ppm) and color coded to Cu content clearly shows that high Pd, low Os sulfides are also high in Cu.

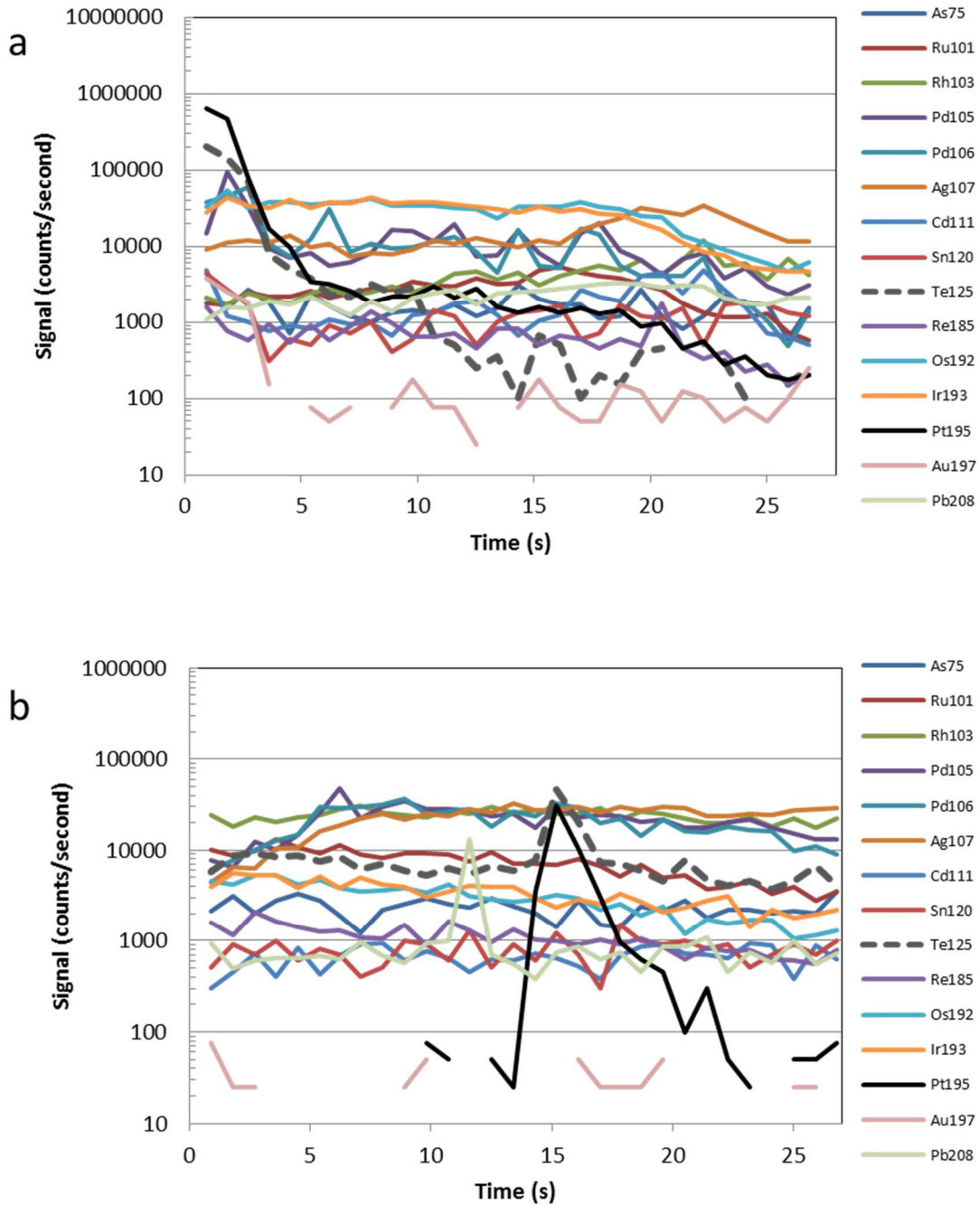


Figure 4.5.1 – Time-resolved laser ablation spectra for individual pentlandite grains. a) A Pt-Pd-Te-Au nugget was just caught at the beginning of ablation at ~1-5 seconds, after which signals stabilize. b) Relatively homogenous PGE signals followed by a sharp Pt spike at ~16 seconds. A Te peak coincides with Pt in this pentlandite. A small spike in Pb is also observed at ~12 seconds.

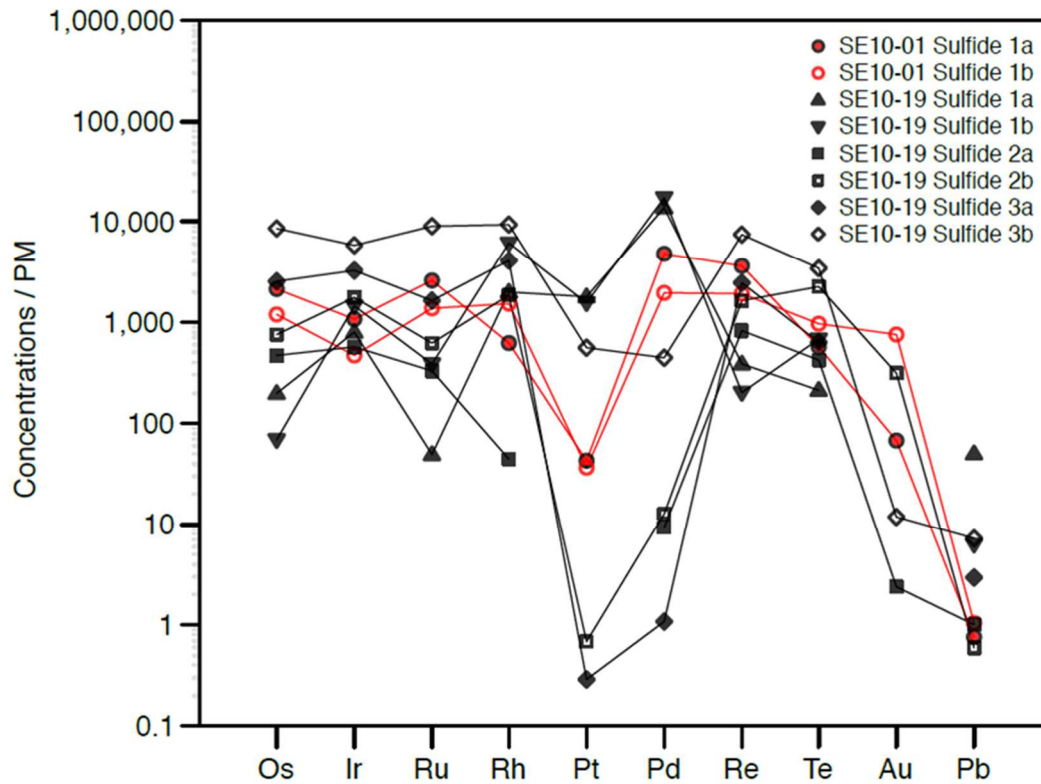


Figure 4.6.1– Included sulfide PGE concentrations normalized to PM. PGE abundance in included sulfides is very similar to interstitial sulfides. Like-symbolled patterns are two adjacent ablation spots in the same sulfide, to test for heterogeneity. The sulfide in SE10-01 and sulfides 1 and 2 in SE10-19 show relatively homogenous PGE concentrations. Pt and Pd in SE10-19 sulfide 3 vary by 3-4 orders of magnitude within $\sim 30 \mu\text{m}$. Error bars are smaller than symbol size. Normalization to PM is equal to Figure 7. Peridotite samples are colored as in Figure 2, symbols differ from Figure 2.

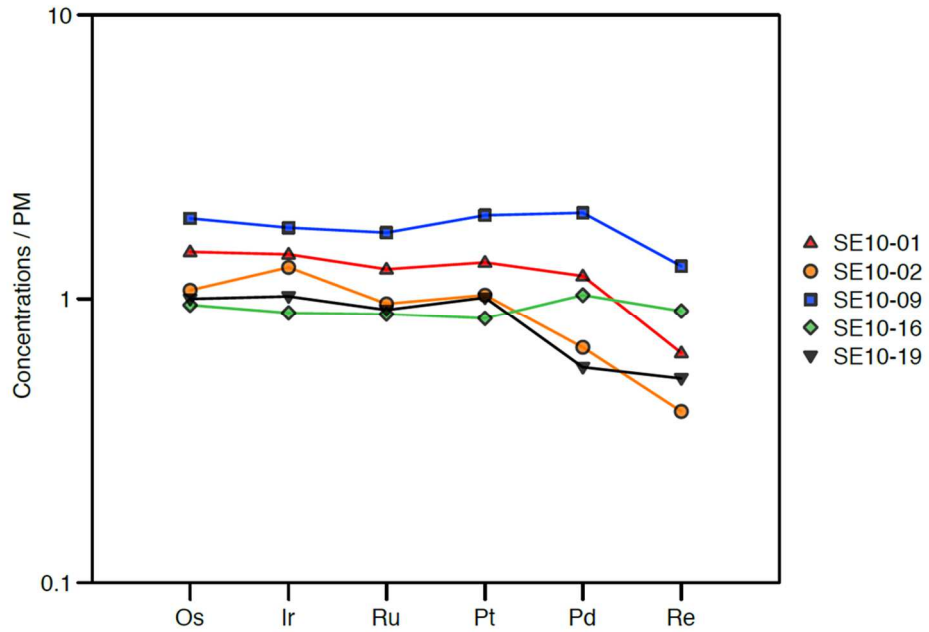


Figure 4.7.1 – Bulk rock PGE concentrations normalized to PM, separated by sample. Colors and symbols are the same as Figure 2. Measured bulk rock concentrations are nominally flat and close to PM values.

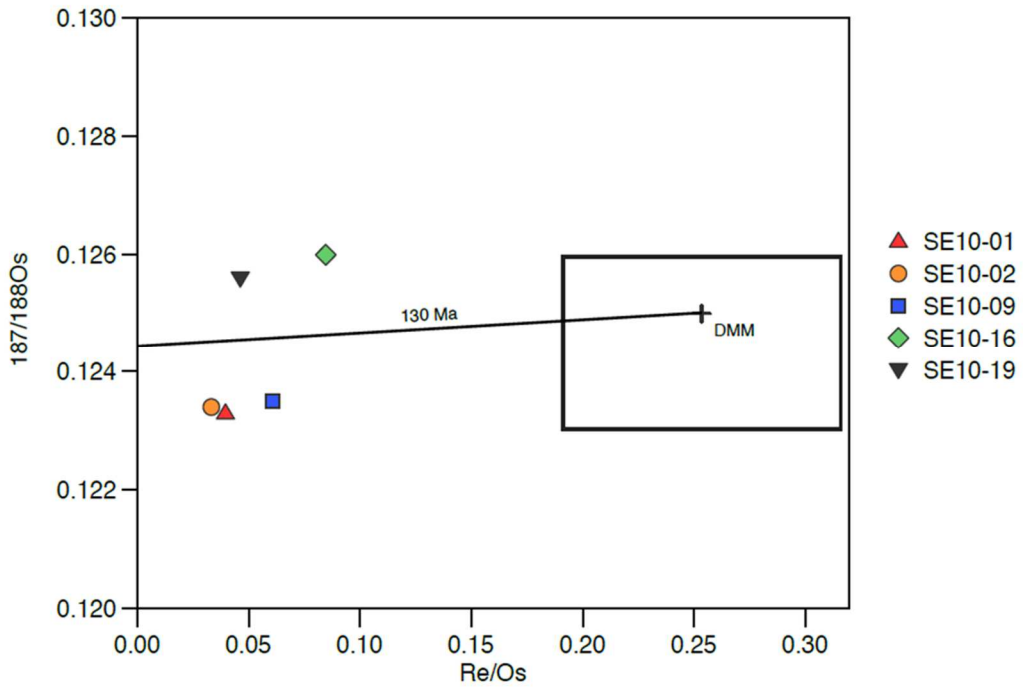


Figure 4.8.1 – $^{187}\text{Os}/^{188}\text{Os}$ of the bulk peridotites compared to the Re/Os measured in the bulk rock. The range and average of Depleted MORB Mantle (DMM) $^{187}\text{Os}/^{188}\text{Os}$ and Re/Os is given for reference. A 130 Ma isochron is plotted, representative of the age at which the St. Elena ophiolite massif is said to have cooled. St. Elena peridotites straddle this isochron.

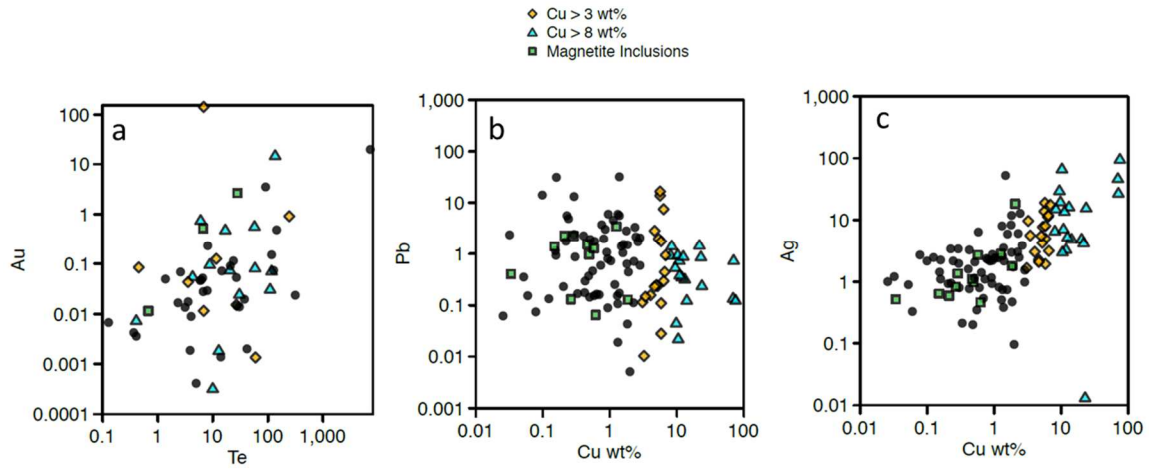


Figure 4.9.1 – Chalcophile element comparisons, with trace elements reported in ppm and Cu in wt%. a) Some correlation between Au and Te is shown. Au and Te concentrations do not correlate with Cu. b) Pb does not correlate with Cu. c) Ag and Cu show excellent correlation, neglecting the low Ag-high Cu outlier.

Chapter 5 Discussion

Here I summarize the key observations from our coupled in situ and bulk rock analyses on PGE systematics.

- Pt depletions are nearly ubiquitous in these peridotites, both lherzolite and harzburgite.
- Pt depletions (and for that matter, enrichments) are observed in all sulfide mineralogies present (i.e. pentlandite, pentlandite with awaruite, pentlandite with native Cu).
- There is a large discrepancy between measured bulk rock and average sulfide Pt concentrations, where the Pt depletions dominantly present in sulfides are absent in the bulk rock.
- Discrete, micron-sized Pt-Te-Au and Cu-Pt-Pd alloys were observed under SEM, and inferred from the occasional spikes in the transient LA-ICPMS signals, as well as micron-sized variability between adjacent ablation spots within single sulfides.

5.1 Pt Anomalies in Sulfides

In order to quantify the extent of Pt depletions, Pt/Pt^* is used as a measure of the Pt anomaly in sulfides. Pt anomaly is quantified as the ratio of the Pt concentration relative to a hypothetical Pt concentration which would plot at the midpoint between neighboring PGE on a primitive mantle normalized plot (e.g. Figure 4.4.1) as:

$$\text{Pt/Pt}^* = \frac{\text{Pt}_{PM}}{(\text{Pd}_{PM} + \text{Ru}_{PM})/2}$$

Note that due to the possible interference of $^{63}\text{Cu}^{40}\text{Ar}$ on Rh, Ru is used in the Pt/Pt* calculation. Pt depletions are nearly ubiquitous and only 8 out of 114 sulfides show positive Pt anomalies. All Pt-enriched sulfides have discrete time-resolved laser ablation spectra showing transient spikes in Pt when spikes in other PGE are absent (e.g. Figure 4.5.1). To a first approximation this suggests that Pt is decoupled from the other PGE on the length scale of tens of microns or even the size of the beam.

To better understand the mechanism which is controlling Pt concentrations in these samples, sulfides with Pt-enriched patterns are more closely examined (Figure 5.1.1). Only 2 of the Pt-enriched sulfides have intermediate or high Cu concentrations (6.9 and 23.8 wt%, respectively). A Cu-poor sulfide in SE10-01 (closed red symbol) is enriched in Te as well as Pt. The time-resolved spectra for this sulfide are shown in Figure 4.5.1a, with positive Pt and Te spikes at the beginning of the ablation signal. Sulfide 1 in SE10-02 (open orange symbol) has a high Cu concentration, and high Pt and Te relative to IPGE. Sulfide 2 in SE10-02 (closed orange symbol) has the highest Pt concentration (902.6 ppm) observed in any sulfide. This sulfide is low in Pd compared to IPGE, but enriched in Te and Au. Spikes in Pt, Te, and Au in the time-resolved ablation signal suggest that a Pt-Te-Au nugget was ablated here. Sulfide 1 in SE10-09 (open blue symbol) has a low Cu concentration. PPGE in this sulfide are high, along with Rh and Te. A PPGE+Rh+Te nugget was possibly ablated here, adjacent to a typical Pt-depleted pentlandite, as another ablation spot adjacent to this one in the same sulfide showed similar IPGE concentrations, and much lower PPGE concentrations (Figure 5.1.2). Pt

enrichment in the Cu-poor Sulfide 2 in SE10-09 (closed blue symbol) is very slight. Re, Te, and Au are all enriched relative to PGE, as PGE in this sulfide are relatively low. Pt-enrichment observed in the Cu-poor Sulfide 1 in sample SE10-16 (open green symbol) is accompanied by high Re concentrations. Another Cu-poor pentlandite (Sulfide 2; closed green symbol) in SE10-16 is slightly enriched in Pt and Rh and depleted in Pd. Te in this sulfide has a negative anomaly in comparison to Re and Au. The only pentlandite in SE10-19 that is not depleted in Pt has a very small Pt enrichment (closed black symbol). Te and Au are also enriched in this sulfide, while Cu has an intermediate concentration. To summarize, Pt enrichments in these sulfides are often found along with Te, Au enrichments, and to a lesser extent Pd, Re, Rh, and Cu. Positive Pt anomalies are not found in conjunction with Os, Ir, or Ru enrichments.

No relationship exists between Pt/Pt* and other PGE, such as Ir or Pd, yet a very tight correlation exists between Pt/Pt* and Pt (Figure 5.1.3a-c). This suggests that Pt concentrations vary independently of other PGE. Further, the relationship between Pt anomalies and Te (and to a lesser extent, Au and Cu) that is observed in extended PGE patterns is clear when Pt/Pt* is plotted against Te, Au, and Cu concentrations (Figure 5.1.3d-f). Rare micron-sized Pt-Te and Pt-Te-Au (and Cu-Pt-Pd-Te-Au) alloys were observed under SEM analysis (Figure 4.2.2), which provides further support to the relationship seen between Pt and those semi-metals. The relationship that exists between Pd and Cu is not abundantly clear in PGE patterns colored coded to Cu content, though a weak correlation does exist. Low-Os, high-Pd sulfides correlate positively with Cu concentrations (Figure 4.4.2a-c).

5.2 Bulk vs. In Situ PGE

There is a stark contrast between bulk rock and sulfide PGE systematics in regard to Pt distribution (Figure 5.2.1). Pt depletions dominant in the sulfides are absent in the bulk rocks. In order to test whether the analyzed sulfide PGE concentrations accurately reflect the bulk rock PGE budget, mass balance reconstructions using in situ sulfide data and bulk rock sulfide S concentrations (Schwarzenbach et al., 2016) were made using two different methods (Table 4.7.1). In the first, the “average” sulfide composition is calculated for each peridotite by averaging out the sulfides and excluding anomalously high PGE concentrations from the average sulfide calculation. In the second method, those outliers are included in the “average” sulfide. Bulk sulfide S concentration is then used to calculate the modal abundance of sulfide (Schwarzenbach et al., 2016), assuming 33.23 wt% of S in the average pentlandite, which is the dominant sulfide phase in these peridotites. If the bulk rock PGE concentrations are controlled by analyzed sulfides, then the product of sulfide modal abundance times sulfide concentration should match the bulk rock concentration. The filtered sulfide reconstructed bulk rock concentrations reasonably reproduce the measured bulk rock Os, Ir, Ru, and to a lesser extent Pd concentrations in these peridotites (Figure 5.1.2a), supporting this approach of a mass balance calculation. Pt, however, is highly underestimated in the reconstructed composition using the filtered data. By including what are assumed to be PGE-rich nuggets, unfiltered reconstructed concentrations can better reproduce Pt concentrations measured in the bulk rock (Figure 5.1.2b). Here, however, IPGE budgets for SE10-02 and SE10-16 are overestimated, due to the high IPGE concentrations found in two ablated phases in each sample (Figure 4.4.1), which dominate the average sulfide

composition. Moreover, samples SE10-01 and SE10-19 still retain a Pt depletion. Therefore, by including PGE-enriched phases in reconstruction calculations, the Pt discrepancy is reduced (or even overcorrected), though this method may generate enrichments in other PGE which are not observed in the bulk rock. At most, 2 PGE-enriched sulfides are included in the unfiltered reconstructions for a given sample. It is possible that the PGE concentrations found in these enriched sulfides are dominated by sulfur-poor nuggets, which are assigned an incorrect sulfur concentration during reconstruction calculations. This misappropriation of sulfur therefore increases the PGE concentration of the average sulfide in a given sample. For example, if an Os-Ir-Ru nugget which contains no sulfur were to be ablated, weighing this nugget equally to normative sulfides would falsely increase the apparent average PGE concentration. Though PGE nuggets may be incorrectly weighted, the fact remains that Pt depletions appear to be related to nugget effects.

5.3 Metasomatic Sulfides

Some sulfides (~5% of the total population) have low IPGE and elevated PPGE, though Pt remains depleted (Figure 5.3.1a). These sulfides (arbitrarily defined here as $Pd/Ir_{PM} > 1$, where $Ir_{PM} < 100$ and $Pd/Os_{PM} > 1$, where $Os_{PM} < 100$) are possibly of a melt-derived origin, as PPGE are more incompatible than IPGE and enriched in melt derived sulfides (Bockrath et al., 2004; Sen et al., 2010). A ~50 μ m native Cu grain found in SE10-09 is an example of a possibly melt-derived sulfide (Figure 4.2.1d; Figure 5.3.1a in blue). This native Cu grain has high Rh, Pt, Pd, Te, and Au concentrations. The Ag concentration is also high, though Pb is not. While this grain did not meet the criteria to which sulfides are screened for metasomatism, it is included in Figure 5.3.1 because of

the abundant presence of chalcophile elements such as Cu, Te, Au, and Ag, which suggests a melt-derived origin. The elevated Rh in this case is likely due to the high $^{63}\text{Cu}^{40}\text{Ar}$ interference from 75.9 wt% Cu in that ablation spot.

Due to the way by which sulfides were screened for metasomatism, two sulfides with extremely fractionated Os/Ir ratios are included in the metasomatized group, though these sulfides are not strictly metasomatic, as PPGE are not enriched relative to Os, Ru, or Rh but the Ir concentrations are very low and decoupled from Os (Figure 5.3.1a). Other sulfides, classified either as metasomatic (Figure 5.3.1a) or non-metasomatic (Figure 4.4.1), also show variable decoupling between Os and Ir as well; this fractionation is highlighted in Figure 5.3.1a. Figures 5.3.1b and c show that the variance in Os/Ir is largely controlled by Ir. One could also argue that decoupling between Ru and Ir is apparent when compared to Ru and Os variations, though Ru/Os and Ru/Ir ratios cluster around PM values (Figure 5.3.1d,e). No known magmatic processes are capable of decoupling Ir from Os in sulfides, because their partition coefficients are similar and high in mantle sulfides (Figure 5.3.2). The mechanism which is fractionating Ir from Os is unclear, but I speculate that it is due to low temperature exsolution processes that may be able to separate Ir from Os (discussed below). No Ir-rich nuggets were evident in the SEM or LA-ICPMS analyses, although this does not exclude their presence.

5.4 Mechanisms of Pt-Decoupling

The abundant presence of sulfides in these samples (up to 188 ppm sulfide sulfur) suggests that desulfurization is not the primary mechanism which created the PGE alloys, as was proposed for the Lherz peridotites by Lugué et al. (2007). Moreover, metasomatism is also unlikely to be responsible for the decoupling of Pt from other PGE

in these samples. First, the relatively unradiogenic Os isotope compositions of these peridotites argue against melt metasomatism. Also, only about 5% of sulfides ablated hold a metasomatic signature with high Pd/Os (and are also largely depleted in Pt), whereas 93% of sulfides have a negative Pt anomaly. Moreover, little evidence of refertilization is found in trace elements of lavas and peridotites sampled from this ophiolite. The partition coefficients during sulfide melting or crystallization are similar for Pt and Pd, (Bockrath et al., 2004; Cafagna and Jugo, 2016; Liu and Brenan, 2015) and for a range of experimental conditions (e.g. Figure 5.3.2). Therefore, melting or crystallization processes cannot decouple Pt from Pd and the other PGE. All these are consistent with limited refertilization and melt interaction, and the presence of Pt depletions in all types of sulfides further argues against melt metasomatism as the mechanism which depleted Pt.

Two scenarios are thus put forth to plausibly explain the Pt depletion in sulfides and the presence of Pt alloys in these peridotites. The first is that Pt alloys are hydrothermally-derived. Schwarzenbach et al. (2014; 2016) suggested that these peridotites experienced hydrothermal fluid infiltration under low water-rock ratios, which could deliver excess volatile chalcophile elements such as Cu, Te, and Au. Bulk rock Cu concentrations, however, do not exceed PM values (Table 4.1.1; McDonough and Sun, 1995). Additionally, mass balance reconstructions for Te and Au show that for the most part these elements are not in excess of primary mantle values (Table 4.7.1; McDonough and Sun, 1995; Godde et al., 2011). An exception to this would be sample SE10-02, which has a definite excess of Te compared to PM. This sample shows some

metasomatic enrichment in trace element concentrations (Figure 4.1.1), therefore the overabundance of Te in this sample could reflect a metasomatic component.

Alternatively, the Pt-Te phases and Pt anomalies could have originated from redistribution of the original PGE and chalcophile element budget of these rocks during magmatic processes other than melting or crystallization. It has been proposed that Pt does not fit into the octahedral site of pentlandite, which leads to its segregation from the pentlandite structure (Luguet et al., 2001; Lorand et al., 2008). Pt-Te-Bi-(Pd) alloys observed in some non-serpentinized peridotites from the Fontête Rouge ophiolite have been thought as the result of subsolidus exsolution from Cu-sulfide melt fractions (Lorand et al., 2008). The possible formation of Pt-Te-Bi-(Pd) phases has been described in Lorand et al. (2008): sulfides should be molten at $1100 \pm 50^{\circ}\text{C}$ at 0.5 Gpa (Bockrath et al., 2004), which is the average pressure of equilibration of the St. Elena peridotites (Madrigal et al., 2015). Upon cooling to 1000°C , a Ni-rich monosulfide solid solution (Mss) is expected to precipitate, as well as a Ni-rich sulfide melt. Pt, Pd, Te, and Cu would preferentially partition into this sulfide melt as soon as Mss starts to crystallize, due to their lower $D^{\text{mss/sulfide melt}} (<0.3; \text{Lorand et al., 2008 and references therein})$. Te and other such semi-metals then form soft ligands with Pt and Pd in the melt (Lorand et al., 2008). Crystallization of Pt-Pd-Te phases is likely achieved at near-sulfide solidus temperature ($850\text{-}890^{\circ}\text{C}$; Peregoedova and Ohnenstetter, 2002) from the last Cu-rich sulfide melt to precipitate (Lorand et al., 2008). Solidification of this Cu-rich sulfide melt produces intermediate solid solution sulfide (Iss), which does not incorporate Pt or Pd ($D^{\text{iss/sulfide melt}} <0.13$ at 840°C ; Lorand et al., 2008 and references therein). Upon further cooling, pentlandite is formed at 610°C , where both Mss and the high temperature

form of heazlewoodite is involved (Guo et al., 1999). Pentlandite can incorporate the majority of PGE into its crystalline structure, though Pt is rejected due to the valence state (0 or +1; Luguét et al., 2001; Lorand et al., 2010). To summarize, Pt-Pd-tellurides may form due to the exclusion of Pt, Pd, Te, and Cu from Iss during crystallization due to the relative incompatibility of these elements in Iss (Peregoedova, 1998; Liu and Brenan, 2015; Cafagna and Jugo, 2016). However, this process cannot cause the decoupling of Pt from Pd that is observed in the St. Elena peridotites because Pt and Pd have similar compatibilities (Figure 5.3.2). Following Luguét et al. (2001) and Lorand et al. (2008), I suggest that upon cooling of these sulfide phases down to 610°C and less, pentlandite incorporates all PGE except for Pt into its crystalline structure, due to a 0 or +1 valence state. Thus, Pt alloy phases which are observed without Pd were formed due to pentlandite crystallization.

The above data suggests that an exsolution origin for the Pt anomalies in the St. Elena mantle sulfides is possible (also Lorand et al., 2010). While the presence of native copper is thought to reflect hydrothermal fluid infiltration (Schwarzenbach et al., 2014), the lack of correlations between Cu and Pt depleted PGE patterns suggest that such fluid did not significantly affect the PGE budget, but likely affected Ag, and possibly Te and Au, based on their correlation with Cu in the LA-ICPMS data.

5.5 A Role for Serpentinization?

The presence of Fe-Ni alloys such as awaruite and native Cu in these samples indicates highly reducing conditions (low fO_2 and fS_2). Schwarzenbach et al. (2014) calculated the stability of native Cu assemblages through Gibbs free energy minimization, and found that native Cu is stable below $-15 \log fS_2$ units and $-30 \log fO_2$

units at 200⁰C and 50 MPa. At the same pressure and at 350⁰C, native Cu was found to be stable below -10 log fS_2 units and -19 log fO_2 units (Schwarzenbach et al., 2014). The coexistence of awaruite with pentlandite further constrains the oxygen and sulfur fugacity conditions for these samples to approximately -16 to -18 log fS_2 units, and -35 to -40 log fO_2 units, based on new experimental data from Foustoukos et al. (2015) at 50 MPa and 300⁰C. These reducing conditions are thought to be the product of low water / rock mass ratios during early stages of serpentinization (Frost, 1985; Klein and Bach, 2009), where olivine hydrolysis releases excess H₂ into the system. Based on the thermodynamic stability of PtS and native Pt, Pt is stable as a native metal at the redox conditions where pentlandite and awaruite exist (log fS_2 < -16 at 300⁰C and 50 MPa; Foustoukos et al., 2015). Thus, while Pt likely exsolved from the Hz-Iss phase and pentlandite due to subsolidus exsolution at ~600-890⁰C, highly reducing conditions during serpentinization allowed for that Pt to remain in its native metal phase and not be incorporated by subsequent sulfides. I speculate that serpentinization and fluid infiltration may have resulted in mobilization and sequestration of Pt into discrete Pt alloys on the sample scale (1 cm). The addition of externally-derived Cu (Schwarzenbach et al., 2015) and possibly Te, Au, and Ag may have resulted in complexation of Pt, and further assisted in the subsequent mobilization and segregation of Pt outside the sulfide structure (Figure 4.2.2a,c). Our mass balance calculations show that only 1-2 Pt-enriched nuggets are needed to mass balance the Pt budget of a rock (high PGE phases in Figure 4.4.1; Figure 5.2.1a vs. 5.2.1b). Pt depletions in mantle peridotitic sulfides have been observed in other peridotites (e.g., Alard et al., 2000; Lorand et al., 2010). Pt enrichments and Pt-alloys have also been observed (e.g., Luguet et al., 2008; Foustoukos et al., 2015). I

suggest that decoupling of Pt into discrete phases separate from other PGE could be a common feature of oceanic lithosphere.

Further, based on the thermodynamic equilibrium of pentlandite and awaruite at 300°C and 50 MPa and the sulfur and oxygen fugacities defined above, Os and Ir are stable as native metals (Foustoukos et al., 2015). In contrast, Ru is stable as a sulfide phase (RuS₂) at the pentlandite-awaruite equilibrium. This provides some evidence that Ir could exist in a native metal phase in these peridotites, suggesting that some “nugget effects” with Ir may well be observed here. Despite not knowing the exact mechanism which decoupled Ir from IPGE, theoretical calculations support our observations (Foustoukos et al., 2015).

5.6 Implications on the Os Isotopic Heterogeneities in the Mantle

The fate of these PGE nuggets upon recycling back into the mantle is uncertain. It is unclear whether the Pt-alloys, as exsolution products, will be re-dissolved into the Mss phase upon peridotite subduction and recycling back into Earth’s mantle, as Pt-tellurides such as moncheite are stable only up to 1150°C (Kim et al., 1990). If extensive serpentinization created disjointed nuggets and sulfides through extensive magnetite veining or desulfurization of the primary sulfides by low fS_2 , perhaps the nuggets would remain in their native state and become trapped by the newly forming magmatic minerals after dehydration of serpentine. Such a process could locally generate excess ¹⁸⁶Os from ¹⁹⁰Pt decay and may contribute to the Os isotopic variability of the upper mantle.

5.7 Pb in Sulfides

Finally, our Pb concentration data on the sulfides allows us to speculate on the fate of Pb in the upper mantle. Hart and Gaetani (2006) calculated that ~75 ppm of Pb has to be held in mantle sulfides in order for sulfides to be the answer to the missing Pb reservoir which counterbalances the radiogenic Pb isotope compositions of MORB and OIB. Sulfides analyzed in these samples do not reach the calculated concentration. Average sulfide Pb concentrations are less than 10% of the 75 ppm that must be held in mantle sulfide (Pb average = 2.2 ppm; range = 0.1-31.6 ppm; n = 114). Further, the calculated Pb budget hosted in the analyzed sulfides (Table 4.7.1) underestimates the measured bulk Pb by 1-2 orders of magnitude. This suggests that sulfides are not the dominant reservoir of Pb in the mantle. Therefore, our data does not support the sulfide solution to the Pb paradox, in agreement with a recent study by Warren and Shirey (2012) on the Pb isotope systematics of sulfides from abyssal peridotites.

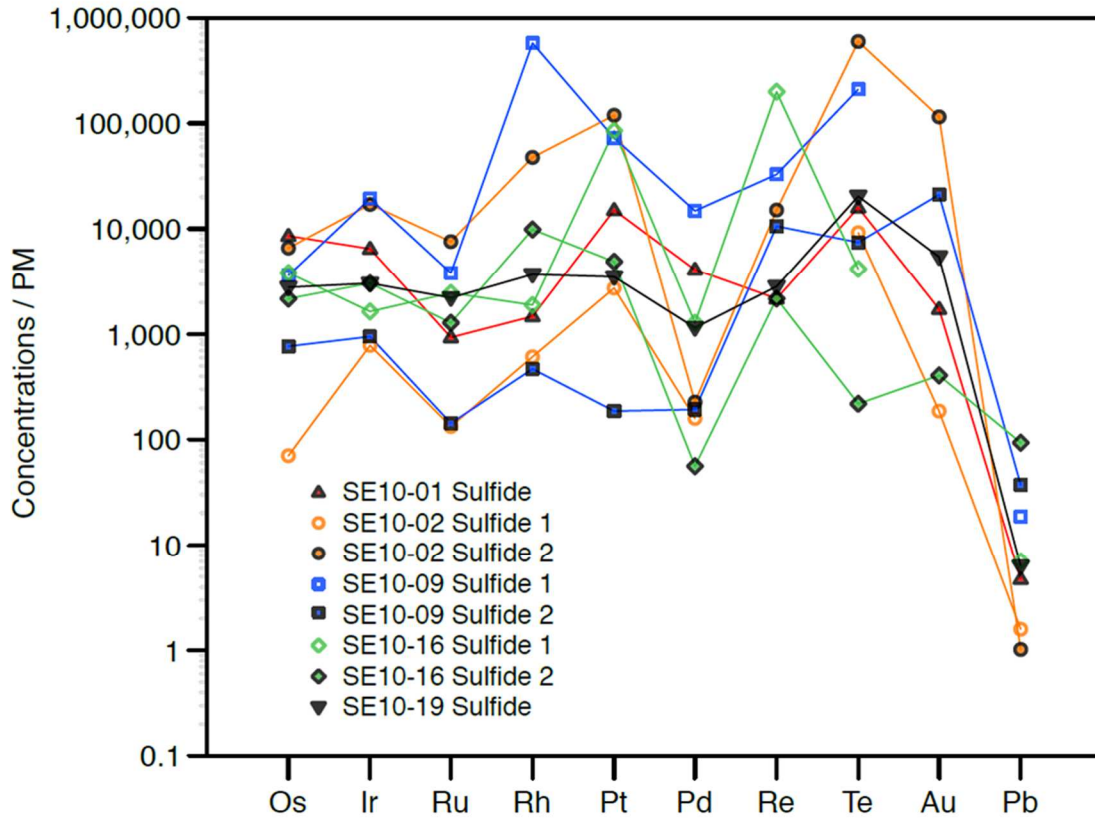


Figure 5.1.1 – Pt enriched sulfide PGE concentrations are shown relative to PM. This figure more visibly illustrates the relationship seen between Pt enrichments and other elements, compared to Figure 8. Sample colors and symbols as in Figure 2. Sulfides from the same sample are distinguished by closed and open symbols.

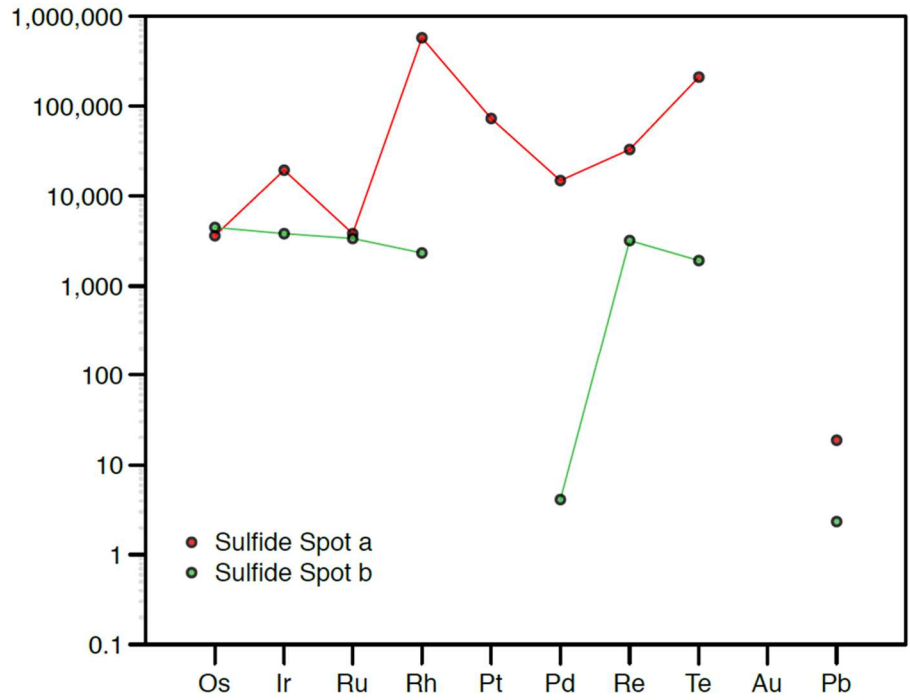


Figure 5.1.2 – PGE concentrations normalized to PM are shown for a particularly heterogeneous sulfide from SE10-09. Rh, Pt, Pd and Te are significantly higher in spot a than in b. Ablation spots were ~30 μm apart.

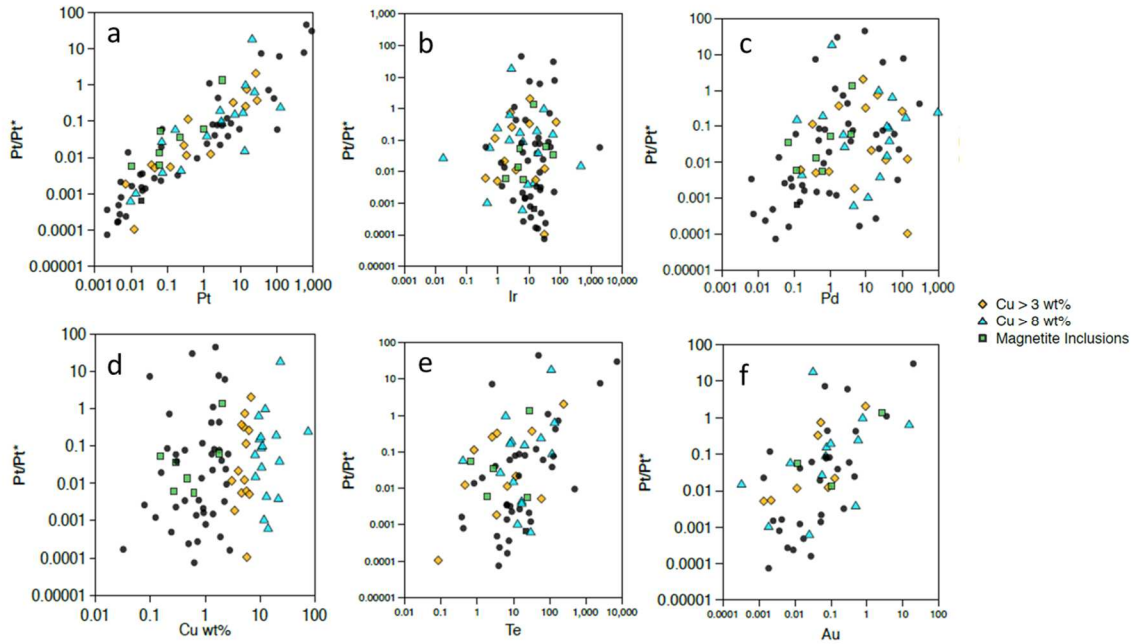


Figure 5.1.3 – Pt/Pt* vs. PGE and chalcophile elements in individual sulfides, color coded to Cu concentrations and magnetite inclusions. Trace elements are shown in ppm. a) Pt anomaly correlates well with Pt. Pt/Pt* does not correlate well with b) Ir or c) Pd. d) No correlation between Pt anomaly and Cu is observed. Pt/Pt* correlates well with e) Te and f) Au.

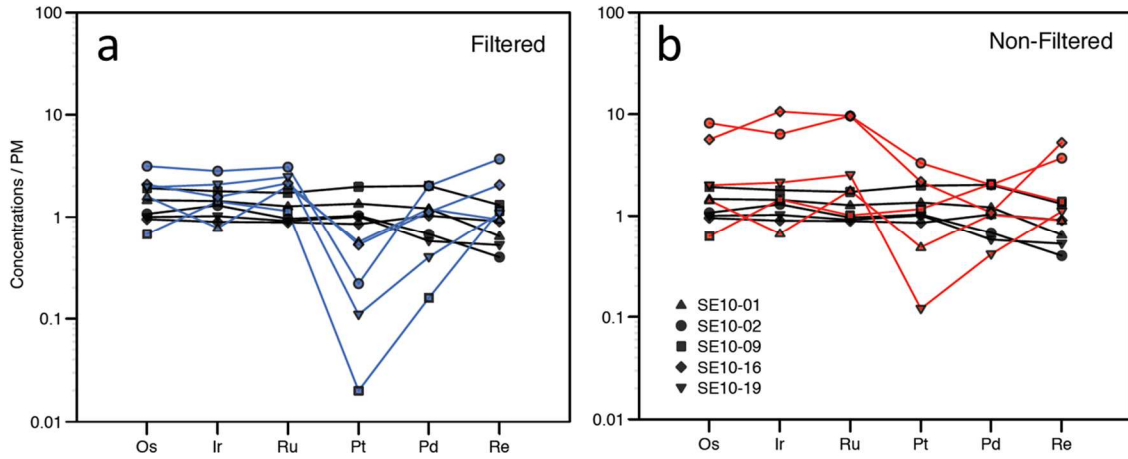


Figure 5.2.1 – Bulk rock PGE measurements compared to a) filtered reconstructed PGE concentrations, shown in blue, and b) non-filtered reconstructed PGE concentrations in the bulk rock, shown in red. Samples are designated by symbols as shown in the legend. Reconstructed concentrations were calculated using averaged in-situ sulfide concentrations, sulfide S concentrations from Schwarzenbach et al. (2016), and an average S concentration for pentlandite of 33.23 wt%. Filtered reconstruction concentrations used average in-situ sulfide concentrations that excluded any obvious nugget phases. Non-filtered reconstructions used the entirety of the sulfide data set for a particular sample. Only 1-2 PGE-enriched phases are excluded from the filtered reconstruction calculations that are included in non-filtered data sets.

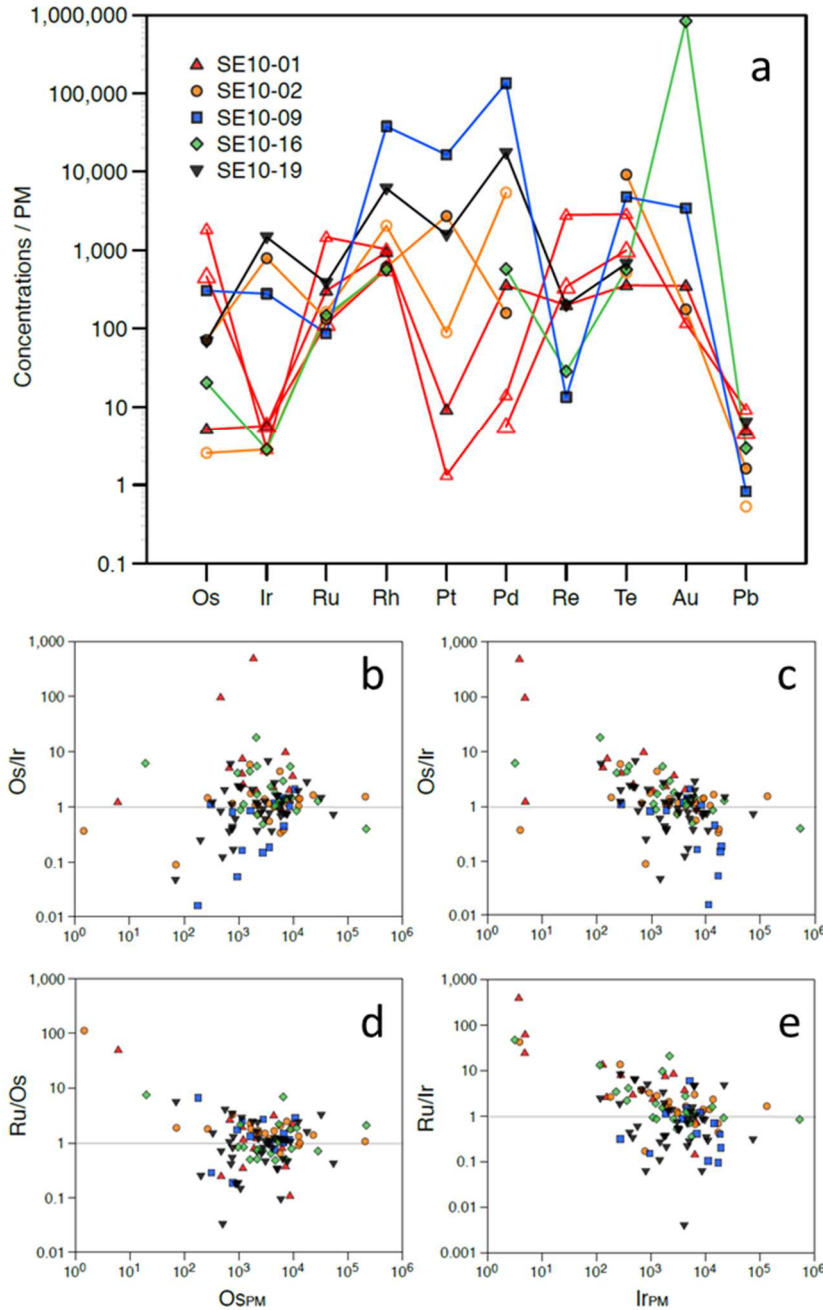


Figure 5.3.1 – a) PM-normalized PGE concentrations for sulfides screened as metasomatic based on their Pd/Ir and Pd/Os ratios. Metasomatic sulfides include a ~50 μm native Cu grain shown in the blue closed square. Pattern colors are as in Figure 2. Symbols size and fill change with respect to the ablated sulfide in a single sample. b-e) IPGE concentration comparisons. PM-normalized Os is compared to b) Os/Ir and d) Ru/Os. PM-normalized Ir is compared to c) Os/Ir and e) Ru/Ir. The tighter correlations between Ir and Os/Ir and Ru/Ir ratios are taken to suggest fractionation or mobilization of Ir relative to Os and Ru.

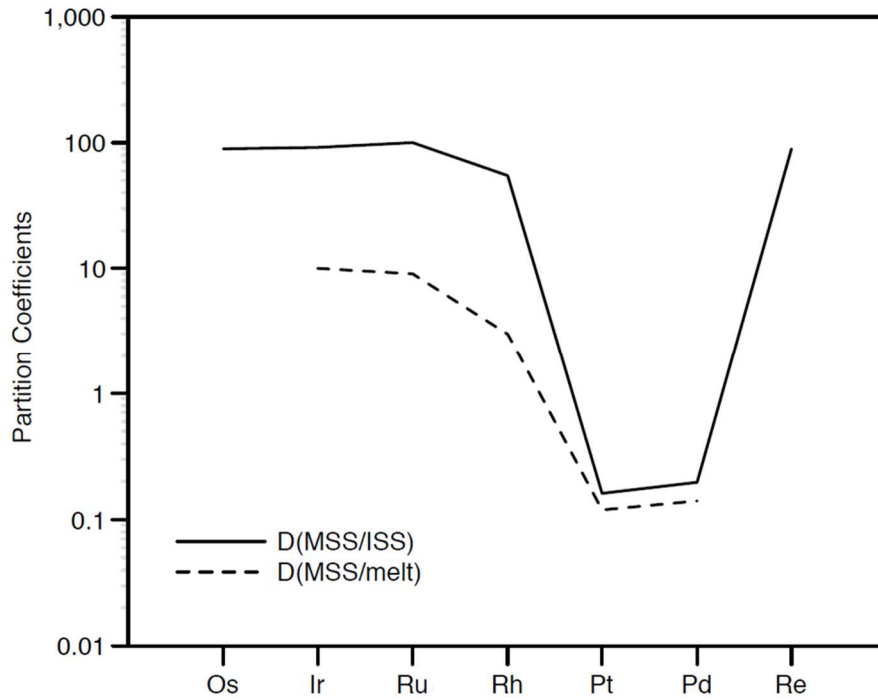


Figure 5.3.2 – MSS/ISS and MSS/melt partition coefficients for PGE-Re. Note the very similar partition coefficients between both Os and Ir, and Pt and Pd. $D(\text{MSS/ISS})$ from Liu and Brenan, 2015; $D(\text{MSS/melt})$ from Bockrath et al., 2004.

Chapter 6 Conclusions

The combined study of in situ LA-ICPMS PGE and chalcophile element concentrations in sulfides, with bulk rock PGE and trace element concentrations in peridotites from the St. Elena ophiolite has shown that Pt is decoupled from the other PGE in sulfides, demonstrated by large depletions. The absence of Pt depletions in the bulk samples, and the identification of Pt-rich alloy phases by SEM and indirectly by LA-ICPMS data suggests that, in these peridotites, a significant part of the Pt budget is primarily held in “nugget” phases. Os, Ir and Ru are primarily held in sulfides, though some variability between Os and Ir seems to be related to an Ir-“nugget effect” as well. A significant fraction of Pd is held in sulfides, though Pd was also recognized in alloy phases. SEM and LA-ICPMS data suggests that Pt mobilization occurs on a fine length scale (microns), which does not extend to the length scale of the bulk rock. Melt depletion resulted in slightly depleted bulk rock PPGE, which suggests that the bulk PGE concentrations are controlled by primary magmatic processes. In turn, the large range of PGE concentrations and the dominant Pt depletions in the sulfides as well as the various PGE-rich alloy phases recognized with the sulfides suggest that the PGE distribution within individual sulfides is a more sensitive indicator of subsolidus processes. I conclude that the distribution of PGE in these sulfides reflects a combination of primary magmatic processes and subsequent fractionation due to subsolidus processes and sulfide mineralogical variability, while the bulk rock PGE distribution is more informative of melting and/or metasomatism. It is likely that in these peridotites, Pt is preferentially

rejected by the pentlandite structure during cooling and recrystallization of the primary mantle sulfides. The low sulfur and oxygen fugacities imposed on these peridotites by subsequent serpentinization allow the stability of Pt as metal alloys and perhaps sequestration of Pt outside the sulfides with the aid of fluids. These findings suggest that the decoupling of Pt into nugget phases could be a common occurrence in oceanic lithosphere. This decoupling of Pt from Re and Os may have implications on the Pt-Re-Os decay system, and may contribute to Os isotopic anomalies in the upper mantle. Finally, this work also finds that sulfides have low Pb concentrations in mantle peridotites, making it unlikely that sulfides are the dominant Pb reservoir in the mantle.

References

- Alard, O., Griffin, W. L., Lorand, J. P., Jackson, S. E., & O'Reilly, S. Y. (2000). Non-chondritic distribution of the highly siderophile elements in mantle sulphides. *Nature*, *407*(6806), 891-894.
- Becker, H., Horan, M. F., Walker, R. J., Gao, S., Lorand, J. P., & Rudnick, R. L. (2006). Highly siderophile element composition of the Earth's primitive upper mantle: constraints from new data on peridotite massifs and xenoliths. *Geochimica et Cosmochimica Acta*, *70*(17), 4528-4550.
- Bockrath, C., Ballhaus, C., & Holzheid, A. (2004). Fractionation of the platinum-group elements during mantle melting. *Science*, *305*(5692), 1951-1953.
- Cafagna, F., & Jugo, P. J. (2016). An experimental study on the geochemical behavior of highly siderophile elements (HSE) and metalloids (As, Se, Sb, Te, Bi) in a mss-iss-pyrite system at 650° C: A possible magmatic origin for Co-HSE-bearing pyrite and the role of metalloid-rich phases in the fractionation of HSE. *Geochimica et Cosmochimica Acta*, *178*, 233-258.
- Delpech, G., Lorand, J. P., Grégoire, M., Cottin, J. Y., & O'Reilly, S. Y. (2012). In-situ geochemistry of sulfides in highly metasomatized mantle xenoliths from Kerguelen, southern Indian Ocean. *Lithos*, *154*, 296-314.
- Foustoukos, D. I., Bizimis, M., Frisby, C., & Shirey, S. B. (2015). Redox controls on Ni-Fe-PGE mineralization and Re/Os fractionation during serpentinization of abyssal peridotite. *Geochimica et Cosmochimica Acta*, *150*, 11-25.
- Frisby, C., Bizimis, M., & Mallick, S. (2016). Seawater-derived rare earth element addition to abyssal peridotites during serpentinization. *Lithos*, *248*, 432-454.
- Garuti, G., & Zaccarini, F. (1997). In situ alteration of platinum group minerals at low temperature: evidence from serpentinized and weathered chromitite of the Vourinos Complex, Greece. *The Canadian Mineralogist*, *35*(1), 611-626.
- Gaboardi, M., & Humayun, M. (2009). Elemental fractionation during LA-ICP-MS analysis of silicate glasses: Implications for matrix-independent standardization. *Journal of Analytical Atomic Spectrometry*, *24*(9), 1188-1197.

- Fischer-Gödde, M., Becker, H., Wombacher, F., & Lorand, J. (2008). Rhodium, gold and other highly siderophile element abundances in terrestrial peridotites. *Geochimica et Cosmochimica Acta Supplement*, 72, 273.
- Hart, S. R., & Gaetani, G. A. (2006). Mantle Pb paradoxes: the sulfide solution. *Contributions to Mineralogy and Petrology*, 152(3), 295-308.
- Hellebrand, E., Snow, J. E., Dick, H. J., & Hofmann, A. W. (2001). Coupled major and trace elements as indicators of the extent of melting in mid-ocean-ridge peridotites. *Nature*, 410(6829), 677-681.
- Kim, W. S., Chao, G. Y., & Cabri, L. J. (1990). Phase relations in the Pd-Te system. *Journal of the Less Common Metals*, 162(1), 61-74.
- Kimura, K., Lewis, R.S., Anders, E., 1974. Distribution of gold and rhenium between nickel – iron and silicate melts: implications for the abundances of siderophile elements on the earth and moon. *Geochim. Cosmochim. Acta* 38, 683–701.
- Kodolányi, J., Pettke, T., Spandler, C., Kamber, B. S., & Gméling, K. (2011). Geochemistry of ocean floor and fore-arc serpentinites: constraints on the ultramafic input to subduction zones. *Journal of Petrology*, egr058.
- Li, C., & Ripley, E. M. (2006). Formation of Pt–Fe alloy by desulfurization of Pt–Pd sulfide in the J–M reef of the Stillwater complex, Montana. *The Canadian Mineralogist*, 44(4), 895-903.
- Liu, Y., & Brenan, J. (2015). Partitioning of platinum-group elements (PGE) and chalcogens (Se, Te, As, Sb, Bi) between monosulfide-solid solution (MSS), intermediate solid solution (ISS) and sulfide liquid at controlled fO₂–fS₂ conditions. *Geochimica et Cosmochimica Acta*, 159, 139-161.
- Lorand, J. P., Delpech, G., Grégoire, M., Moine, B., O'Reilly, S. Y., & Cottin, J. Y. (2004). Platinum-group elements and the multistage metasomatic history of Kerguelen lithospheric mantle (South Indian Ocean). *Chemical Geology*, 208(1), 195-215.
- Lorand, J. P., Luguét, A., & Alard, O. (2008). Platinum-group elements: a new set of key tracers for the Earth's interior. *Elements*, 4(4), 247-252.
- Lorand, J. P., Luguét, A., Alard, O., Bezos, A., & Meisel, T. (2008). Abundance and distribution of platinum-group elements in orogenic lherzolites; a case study in a Fontete Rouge lherzolite (French Pyrénées). *Chemical Geology*, 248(3), 174-194.

- Lorand, J. P., Alard, O., & Luguet, A. (2010). Platinum-group element micronuggets and refertilization process in Lherz orogenic peridotite (northeastern Pyrenees, France). *Earth and Planetary Science Letters*, 289(1), 298-310.
- Luguet, A., Alard, O., Lorand, J. P., Pearson, N. J., Ryan, C., & O'Reilly, S. Y. (2001). Laser-ablation microprobe (LAM)-ICPMS unravels the highly siderophile element geochemistry of the oceanic mantle. *Earth and Planetary Science Letters*, 189(3), 285-294.
- Luguet, A., Shirey, S. B., Lorand, J. P., Horan, M. F., & Carlson, R. W. (2007). Residual platinum-group minerals from highly depleted harzburgites of the Lherz massif (France) and their role in HSE fractionation of the mantle. *Geochimica et Cosmochimica Acta*, 71(12), 3082-3097.
- Luguet, A., Pearson, D. G., Nowell, G. M., Dreher, S. T., Coggon, J. A., Spetsius, Z. V., & Parman, S. W. (2008). Enriched Pt-Re-Os isotope systematics in plume lavas explained by metasomatic sulfides. *Science*, 319(5862), 453-456.
- Madrigal, P., Gazel, E., Denyer, P., Smith, I., Jicha, B., Flores, K. E., ... & Snow, J. (2015). A melt-focusing zone in the lithospheric mantle preserved in the Santa Elena Ophiolite, Costa Rica. *Lithos*, 230, 189-205.
- McDonough, W. F., & Sun, S. S. (1995). The composition of the Earth. *Chemical geology*, 120(3), 223-253.
- O'Neill, H. S. C. (1990). Oxygen fugacity and siderophile elements in the Earth's mantle: Implications for the early history of the earth. *Meteoritics*, 25, 395.
- Peregoedova, A., & Ohnenstetter, M. (2002). Collectors of Pt, Pd and Rh in a S-poor Fe–Ni–Cu sulfide system at 760 C: experimental data and application to ore deposits. *The Canadian Mineralogist*, 40(2), 527-561.
- Peregoedova, A., Barnes, S. J., & Baker, D. R. (2004). The formation of Pt–Ir alloys and Cu–Pd-rich sulfide melts by partial desulfurization of Fe–Ni–Cu sulfides: results of experiments and implications for natural systems. *Chemical Geology*, 208(1), 247-264.
- Schwarzenbach, E. M., Gazel, E., & Caddick, M. J. (2014). Hydrothermal processes in partially serpentinized peridotites from Costa Rica: evidence from native copper and complex sulfide assemblages. *Contributions to Mineralogy and Petrology*, 168(5), 1-21.

- Schwarzenbach, E. M., Gill, B. C., Gazel, E., & Madrigal, P. (2016). Sulfur and carbon geochemistry of the Santa Elena peridotites: Comparing oceanic and continental processes during peridotite alteration. *Lithos*.
- Sen, I. S., Bizimis, M., & Sen, G. (2010). Geochemistry of sulfides in Hawaiian garnet pyroxenite xenoliths: implications for highly siderophile elements in the oceanic mantle. *Chemical Geology*, 273(3), 180-192.
- Shirey, S. B., & Walker, R. J. (1998). The Re-Os isotope system in cosmochemistry and high-temperature geochemistry. *Annual Review of Earth and Planetary Sciences*, 26(1), 423-500.
- Warren, J. M., & Shirey, S. B. (2012). Lead and osmium isotopic constraints on the oceanic mantle from single abyssal peridotite sulfides. *Earth and Planetary Science Letters*, 359, 279-293.